RESEARCH

Macrophage extracellular vesicle-packaged miR-23a-3p impairs maintenance and angiogenic capacity of human endothelial progenitor cells in neonatal hyperoxia-induced lung injury

Xuan Wang[1], Fang Yao[1], Lingling Yang[1], Dongshan Han[1], Yali Zeng[1,2], Zilu Huang[1], Chuanzhong Yang[1,2,3], Bingchun Lin[1*] and Xueyu Chen[1,2,3*]

Abstract

Background Premature infants requiring mechanical ventilation and supplemental oxygen for respiratory support are at increased risk for bronchopulmonary dysplasia (BPD), wherein inflammation have been proposed as a driver of hyperoxia-induced injuries, including persistent loss of endothelial progenitor cells (EPCs), impaired vascularization and eventual alveolar simplification in BPD lungs. However, the underlying mechanisms linking these phenomena remain poorly defined.

Methods We used clodronate liposomes to deplete macrophages in a mouse model of neonatal hyperoxia-induced lung injury to evaluate if EPC loss in BPD lungs could be an effect of macrophage infiltration. We further generated in vitro culture systems initiated with cord blood (CB)-derived CD34$^+$ EPCs and neonatal macrophages either polarized from CB-derived monocytes or isolated from tracheal aspirates of human preterm infants requiring mechanical ventilation and oxygen supplementation, to identify EV-transmitted molecular mechanism that is critical for inhibitory actions of hyperoxic macrophages on EPCs.

Results Initial experiments using mouse model identified the crucial role of macrophage infiltration in eliciting significant reduction of c-Kit$^+$ EPCs in BPD lungs. Further examination of this concept in human system, we found that hyperoxia-exposed neonatal macrophages hamper human CD34$^+$ EPC maintenance and impair endothelial function in the differentiated progeny via the EV transmission of *miR-23a-3p*. Notably, treatment with antagomiR-23a-3p to silence *miR-23a-3p* in vivo enhances c-Kit$^+$ EPC maintenance, and increases capillary density, and consequently mitigates simplified alveolarization in BPD lungs.

Conclusion Our findings highlight the importance of pulmonary intercellular communication in the pathophysiology of BPD, by identifying a linkage through vesicle transfer of *miR-23a-3p* from hyperoxic macrophages to EPCs, and thus demonstrating potential for novel therapeutic target in BPD.

*Correspondence:
Bingchun Lin
pureice1998268@126.com
Xueyu Chen
snowvsrain@smu.edu.cn
Full list of author information is available at the end of the article

Wang *et al. Stem Cell Research & Therapy*   (2024) 15:295

Page 2 of 22

Introduction

Advancements in modern perinatal and neonatal intensive care have improved the survival of infants born at very low gestational age, but postnatal life-saving therapies that rely on mechanical ventilation and supplemental oxygen for respiratory support can also cause injuries to the immature lungs and contribute to increased occurrence of bronchopulmonary dysplasia (BPD) [1]. BPD is a chronic lung disease characterized by impaired vascularization, arrested alveolarization and reduced lung function that may persist beyond adolescence [1–4]. Despite significant advances in improving neonatal management over the past decades, BPD remains the most common complication among extremely preterm infants [1] and thus, there is still an urgent need for identifying new pathologic mechanisms that inhibit vascular and alveolar growth, which may lead to potential novel therapeutics.

Disruption of pulmonary vascularization—resulting in part from persistent loss of endothelial progenitor cells (EPCs) in hyperoxia-injured lungs [5], is an important contributor to the pathophysiology of BPD [6, 7]. In mice, c-Kit$^+$ EPCs which are capable of proliferation, migration to the alveolar vasculature, and further differentiation into mature endothelial lineages, are abundant in fetal lung at homeostasis [5, 8–10]. These capacities of lung cKit$^+$ EPCs to maintain and restore the alveolar microvasculature make them indispensable for lung health and resilience. However, recent work has revealed that prolonged hyperoxia exposure can cause significant loss of c-Kit$^+$ EPCs in mouse BPD lungs, and through adoptive transfer of c-Kit$^+$ EPCs—hyperoxia-injured vascular and alveolar structures could be restored [5]. In humans, circulating EPCs were found to be significantly decreased in blood samples of preterm infants who later developed BPD [11, 12]. Although the clinical efficacy of EPCs has not been tested in BPD yet, human CD34$^+$ EPCs (functionally equivalent to mouse c-Kit$^+$ EPCs) have demonstrated their regenerative activity to improve vascularization and outcomes in clinical trials of other vascular diseases [13–15]. Collectively, these findings underscore the importance of understanding the mechanisms of EPC loss in BPD and developing therapies to circumvent the loss.

Accruing evidence from studies of experimental BPD model and clinical samples has shown that deregulation of macrophages—both recruited and resident, is a leading cause of unrestrained inflammation that also results in the pathogenesis of BPD [16–19]. In addition to the role of being as the key constituent of inflammatory lung environment in response to injury, macrophages have also demonstrated their capacity to modify local environment via production of cytokines, growth factors, and extracellular vesicles (EVs) [18, 20–22]. EVs are biological membrane-bound nanoparticles carrying numerous cargo molecules and are known to play a critical role in mediating cellular communication via transporting lipids, messenger RNAs (mRNAs), microRNAs (miRNAs), and bioactive proteins, to modulate the response of recipient cells [23]. Given that macrophage-derived EVs have the ability to propagate signals and exert biological functions in various lung diseases [21, 24, 25], and furthermore, levels of EVs are elevated in tracheal aspirates (TA) of patients with severe BPD [26], we therefore hypothesize that a mechanistic involvement of macrophage-derived EVs drives the disease progression of BPD.

There is no empirical evidence that EPC loss is linked directly to macrophage-derived EVs in BPD, to our knowledge. In the present study, we identified that hyperoxic macrophages release EV-transmitted *miR-23a-3p* to induce EPC loss and impair endothelial function of the differentiated progeny. Our findings also show that by perturbing *miR-23a-3p* expression in vivo, we can restore EPC maintenance and capillary density, and further enhance alveolarization in hyperoxia-injured lungs. Together, these results underlie the importance of intercellular communication in the response of the lung to prolonged oxygen exposure, and further demonstrate that macrophage-derived EV-encapsulated *miR-23a-3p* has a previously unrecognized role in the pathogenesis of BPD.

Materials and methods

Primary samples

Human CB was obtained from healthy donors and processed within 1 h after the collection. Mononuclear cells (MNCs) were isolated from fresh human CB using Lymphoprep (STEMCELL Technologies) density gradient separation by centrifugation at $800 \times g$ for 20 min.

Tracheal aspirates (TA) were collected from infants admitted to the Shenzhen Maternity & Child Healthcare Hospital Neonatal Intensive Care Unit. Entry criteria included gestational age at birth ≤ 27 weeks, requiring mechanical ventilation for respiratory distress, and postnatal age ≤ 15 days. Aspirates were collected during routine tracheal suctioning of mechanically ventilated premature infants. Collected samples were spun down

Wang *et al. Stem Cell Research & Therapy*   (2024) 15:295

Page 3 of 22

at $400 \times g$ for 5 min to separate cell pellet from supernatant, and non-specific binding was blocked with human TruStain FcX™ [BioLegend # 422302]) for 10 min on ice. $CD14^+$ monocytes and macrophages were then isolated using anti-human CD14 Microbeads (Miltenyi Biotec) according to the manufacturer's instructions. Purity was verified by re-staining isolated cells with anti-human CD11b-FITC antibody (1:100, BioLegend # 301330) and anti-human CD14-APC antibody (1:100, BioLegend #367118), followed by analyzing cells on a Beckman Coulter CytoFLEX flow cytometer.

Purified TA $CD14^+$ monocytes and macrophages (TA-M) were suspended in RPMI supplemented with human GM-CSF (20 ng/mL; Peprotech #300-03), penicillin/streptomycin (P/S; 100 U/mL; Invitrogen #15140122) and 5% EV-depleted FBS (EVs were depleted from FBS by ultrafiltration following the protocol as previously described [27]), and added to the upper chambers of 24 mm Transwell inserts (Corning #3450) with a pore size of 0.4 µm, at 1.5×10^6 cells/insert. 2 mL of RPMI supplemented with human GM-CSF (20 ng/mL) and 5% EV-depleted FBS was also added to the lower chambers. After 24 h of incubation, culture medium from the lower chambers was harvested and precleared by centrifugation at $1000 \times g$ for 10 min, followed by filtering through 0.22 µm filter to proceed as precleared conditioned medium (CM) for downstream CM and EV experiments.

Isolation and expansion of human endothelial cell mixtures and $CD34^+$ EPCs

For human EPCs isolation and culture, protocol from Ravishankar et al. [28] was used with slight modifications. Briefly, CB MNCs were resuspended in EGM-2MV medium (Lonza #CC-3202) supplemented with 5% FBS, 100 U/ml P/S, 2 mM L-glutamine, and 22.5 µg/mL heparin (complete EGM medium) followed by plating on fibronectin-coated plates (fibronectin coated at 2 µg/cm²) at a density of 6×10^6 MNCs per well in a 6-well plate. Media change with complete EGM medium was performed every day for the first 5 days, and then was changed every 3 days afterwards until colonies appeared in culture. Colonies were harvested by trypsinization and $CD31^+$ endothelial cell mixtures (composed of $CD34^+$ EPCs and mature $CD34^-$ endothelial cells) were enriched immunomagnetically using an anti-human CD31 Microbeads (Miltenyi Biotec) according to the manufacturer's instructions (Purity > 95%). Next, purified $CD31^+$ endothelial cell mixtures were plated on fibronectin-coated T75 flasks for further expansion, and harvested for $CD34^+$ EPCs at the end of passage 1 by trypsinization and purification using anti-human CD34 Microbeads (Miltenyi Biotec) according to the manufacturer's instructions (purity was verified > 95%). Purified

$CD34^+$ EPCs at passage 1 were used for downstream experiments.

Human neonatal MDM differentiation and hyperoxia treatment

Neonatal MDM differentiation was performed as previously described [29]. Briefly, CB MNCs were plated to adhere in 150 mm round dishes in RPMI, at a density of 4.0×10^7 cells per dish for 1.5-h to enrich monocytes. Non-adherent cells were then removed by washing with PBS post 1.5-h incubation. Plated monocytes were grown in RPMI supplemented with 10% FBS, followed by differentiation with 20 ng/mL human GM-CSF (Peprotech #300-03) for 5 days, reaching a confluency > 90%. Next, polarized macrophages were exposed to normoxia (NOX; 21% O_2) or hyperoxia (HYX; 60% O_2) for 48 h followed by changing media to RPMI supplemented with human GM-CSF (20 ng/mL) and 5% EV-depleted FBS. Culture supernatant from NOX MDM and HYX MDM cultures (20 mL per 150 mm round dish at a density of $\sim 6 \times 10^6$ macrophages/dish with an average viability > 90% at harvest) was later harvested following 24-h culture and centrifuged at $1000 \times g$ for 10 min to pellet dead cells and debris. The supernatant was then filtered through 0.22 µm filter and proceeded as precleared CM for downstream CM and EV experiments.

Experiments with CM, EV, and EV-depleted CM fractions

For the CM experiments, precleared CM was firstly concentrated by centrifugation using Amicon Ultra filter (10 k Da MWCO; UFC901024) with a cutoff of 10 kDa after centrifugation at $4000 \times g$ for 30 min before supplementing at 1% v/v to the respective complete EGM media for the following treatment on endothelia cell mixtures or $CD34^+$ EPCs (10 mL precleared CM could be concentrated to ~ 100 uL and added at 1% v/v of the complete EGM media). For the EV and EV-depleted CM experiments, precleared CM was firstly ultracentrifuged (CR30NX, Himac) at $100,000 \times g$ for 4 h at 4 °C. The resulting supernatant had been depleted of EVs after 4 h ultracentrifugation, therefore was collected and further concentrated with 10 kDa Amicon Ultra filter (10 k Da MWCO; UFC901024) before adding at 1% v/v to the respective complete EGM media for the EV-depleted CM treatment on $CD34^+$ EPCs (10 mL EV-depleted CM could be concentrated to ~ 100 uL and added at 1% v/v of the complete EGM media). The EV pellets were resuspended in PBS and subsequently supplemented to corresponding to complete EGM media for the EV treatment on $CD34^+$ EPCs (EV pellets were resuspended at 100 uL of PBS per 10 mL starting precleared CM and added at 1% v/v of the complete EGM media).

Wang *et al. Stem Cell Research & Therapy*   (2024) 15:295

Page 4 of 22

For in vitro experiments with CD34$^+$ EPCs, CD34$^+$ EPCs were plated on fibronectin-coated plates at a density of 2000 cells/cm^2 followed by media change the next day with complete EGM media supplemented with respective concentrated CM, EVs, or concentrated EV-depleted CM fractions (all added at 1% v/v of the complete EGM media). Media change with complete EGM media supplemented with respective concentrated CM, EVs, or concentrated EV-depleted CM fractions (all added at 1% v/v of the complete EGM media) was performed on day 4. Primary harvest for the cells from all treated groups was performed by trypsinization on day 7, followed by flow characterization and replating of the cells on fibronectin-coated plates at a density of 4000 cells/cm^2. Replated cells were cultured in complete EGM media supplemented with respective concentrated CM, EVs, or concentrated EV-depleted CM fractions (all added at 1% v/v of the complete EGM media) and media change was performed 4 days later. Harvest for the replated cells (secondary harvest) by trypsinization was conducted at 1-week culture of the replated cells, followed by assessing endothelial function with tube formation assay and migration assay of the harvested cells.

For each media change, same amount of starting precleared CM from macrophage cultures was used to obtain the concentrated CM, EVs, or concentrated EV-depleted CM fractions.

EV characterization

For morphological assessment, 20 uL of fresh EVs were dried on a copper grid for 3 min followed by staining with 3% phosphotungstic acid for 3 min. The EVs were then immediately observed using a transmission electron microscope (HT7700, Hitachi). For quantification of EVs in respective precleared CM, a NanoSight NS300 instrument (Malvern Instruments) equipped with NTA 3.0 analytical software (Malvern Instruments) was used.

For immunoblotting, total protein of cells and EVs was extracted and quantified using a BCA kit (Beyotime #P0009). 15 μg of protein samples were loaded and separated using polyacrylamide gel electrophoresis, followed by transferring onto PVDF membrane (Bio-Rad #1620177). The membranes were blocked with 5% non-fat milk dissolved in TBST (tris-buffered saline (TBS) supplemented with 0.05% tween 20) for 1 h and then were incubated with primary antibodies overnight at 4 °C. Primary antibodies against CD63 (1:200; Santa Cruz # sc-5275), Alix (1:200; Santa Cruz #sc-53540), CD81 (1:1000; CST #56039s), and GM130 (1:1000; CST #124807). After being washed with TBST for three times, membranes were subsequently incubated with corresponding HRP-conjugated secondary antibodies: anti-mouse IgG-HRP (1:3000; CST #7076s), anti-rabbit IgG-HRP (1:3000; CST #7074s) for 1 h and in TBST. Protein bands were visualized after incubation with SuperSignal™ West Pico PLUS Chemiluminescent Substrate (Thermo fisher #34580) and imaged using FluorChem M System (ProteinSimple #92-15312-00).

For visualization of EV internalization, EVs were labelled with 6uM DiO (Invitrogen #V22886) for 15 min at 37 °C, and then quenched with 10%BSA in PBS. To remove remaining dyes, labelled EVs were further washed with PBS and ultracentrifuged at 100,000 ×g for 2 h. Labelled EVs were subsequently added to CD34$^+$ EPCs to evaluate EV uptake. Following incubation overnight at 37 °C, the cells were fixed, stained with Rab7 (1:100; CST #9367) overnight at 4 °C followed by staining with DAPI (Beyotime #C1006) the next day and visualized by confocal microscopy.

Cell and EV transfection with miRNA mimics or inhibitors

For cell transfection, CD34$^+$ EPCs (viability > 95% and purity of CD31$^+$34$^+$ EPCs within live population > 95%) were seeded at 200,000 cells per T25 flask prior to transfection the next day with negative control (NC) mimic or miR-191-5p/miR-532-5p/miR-23a-3p mimic (GenePharma, China) at a concentration of 100 nM using Lipofectamine 3000 (Invitrogen #L3000015) as instructed by the manufacturer's protocols.

Exo-Fect (System Biosciences #EXFT200A-1) was used for EV loading. Briefly, 10^9 EVs were incubated with Exo-Fect transfection reagent and respective 20 uM mimics or inhibitors (NC mimic, or miR-23a-3p mimic, or NC inhibitor, or miR-23a-3p inhibitor), followed by loading onto a clean-up spin-column to remove the remaining Exo-Fect reagent and excess mimics/inhibitors, as instructed by the manufacturer's protocols. The purified transfected EVs were then added to the respective cultures of CD34$^+$ EPCs, which were seeded at a density of 2000 cells/cm^2 in T75 flask. Media change with freshly transfected EVs supplemented was performed every 4 days.

hsa-miR-191-5p mimic (sense: 5′-CAACGGAAU CCCAAAAGCAGCUG-3′, anti-sense: 5′-GCUGCU UUUGGGAUUCCGUUGUU-3′);

hsa-miR-532-5p mimic (sense: 5′-CAUGCCUUG AGUGUAGGACCGU-3′, anti-sense: 5′-GGUCCU ACACUCAAGGCAUGUU-3′);

hsa-miR-23a-3p mimic (sense: 5′-AUCACAUUG CCAGGGAUUUCC-3′, antisense: 5′-AAAUCCCUG GCAAUGUGAUUU-3′)

Wang *et al. Stem Cell Research & Therapy*   (2024) 15:295

Page 5 of 22

hsa-miR-23a-3p inhibitor (5′-GGAAAUCCCUGG CAAUGUGAU-3′)

Transwell migration assay

The migration potential was assessed using Transwell with 8 μm pores (Corning #3422). Briefly, 3×10^4 differentiated progeny of CD34$^+$ EPCs harvested from different conditions suspended in serum-free EGM medium were added to the upper chamber for assessment of chemotaxis toward complete EGM medium (containing FBS) in the lower chamber. After incubation overnight at 37 °C, the cells attached to the upper side were removed, and the cells attached to the bottom side of the membrane were fixed, permeabilized, and stained with DAPI (Beyotime, #P0131-25 ml), followed by imaging using confocal microscopy and quantification of the migrated cell number by ImageJ (Wayne Rasband, National Institute of Health, USA).

Wound healing assay

The migration potential was also assessed using wound healing assay. Briefly, treated CD34$^+$ EPCs were seeded in 12-well plates to create a confluent monolayer. Once they reached 90% confluency, the cell monolayer was firstly treated with mitomycin c (final concentration at 10 μg/mL; AbMole Bioscience #M5791) for 2 h before scratching with a sterile p100 pipette tip, followed by cell washing with PBS twice before changing to complete EGM. Images were acquired using a bright-field microscope at 0 h and 6 h post-scratch induction. Scratched area was measured on ImageJ (Wayne Rasband, National Institute of Health, USA), and the percent wound closure was calculated by (0 h scratched area − 6 h remaining scratched area)/0 h scratched area × 100%.

Tube formation assay

Tube formation assays were performed according to a published protocol [30] with slight modifications. Briefly, 50uL of diluted cultrex reduced growth factor basement membrane extract [(type 2, R&D #3536-005-02) 1:1 diluted with complete EGM] was coated onto each well of a 96-well plate and incubated at 37 °C for an hour until the coated membrane extract solidified. Next, differentiated progeny of CD34$^+$ EPCs (1.25×10^4 cells) were added to the coated wells and incubated at 37 °C for 6 h. Images were taken with a microscope at 100× magnification. The tube formation ability was quantified at 100× magnification using Image J (Wayne Rasband, National Institute of Health, USA) and Angiogenesis Analyzer plugin (Gilles Carpentier, Universite Paris Est Creteil Val de Marne, France).

Flow cytometry

For surface phenotype analyses, harvested cells were resuspended in blocking buffer (4%FBS in PBS supplemented with human TruStain FcX™ [BioLegend # 422302] for human cells or mouse BD Fc Block [BD # 553142] for mouse cells) for 10 min on ice, and then incubated for 30 min in the dark at 4 °C with selected fluorochrome-conjugated antibodies, followed by washing in PBS with 2% FBS, and resuspended in 0.1% PI (1 mg/mL, Sigma #P4170) to detect viable cells. Phenotyping of the cells was performed on a Beckman Coulter CytoFLEX flow cytometer, and data was analyzed on FlowJo v.10 software. For human CD34$^+$ EPC staining panel, cells were stained with the following antibodies: FITC-anti-CD31 (1:100, BioLegend # 303120), and APC-anti-CD34 (1:50, BD Pharmingen #555824). For purity check of human CD14$^+$ monocytes/macrophages isolated from TA samples, cells were stained with the following antibodies: FITC-anti-CD11b (1:100, BioLegend # 301330), APC-anti-CD14 (1:100, BioLegend #367118).

For Ki67 proliferation assay, CD34$^+$ EPC differentiated progeny were resuspended in human blocking buffer for 10 min on ice, and then incubated for 30 min in the dark at 4 °C with APC-anti-CD34 (1:50, BD Pharmingen #555824). After staining, the cells were incubated with fix/perm buffer (Thermo Fisher Scientific #00-5523-00) at room temperature (RT) for 1 h, followed by incubation with permeabilization buffer (Thermo Fisher Scientific #00-5523-00) at RT for 1.5 h. After permeabilization, cells were further stained with an anti-human Ki67-FITC antibody (1:10, FITC Mouse Anti-Ki-67 Set, BD Biosciences #556026) or IgG-FITC control in permeabilization buffer at RT for 1 h prior to flow cytometry analysis. Proliferating human CD34$^+$ EPCs were defined as CD34$^+$ Ki67$^+$.

To detect cell apoptosis, an Annexin V-FITC apoptosis detection kit (BD Pharmingen #556547) was used according to manufacturer's instructions.

For mouse c-Kit$^+$ EPC detection, single cell suspensions from lung were incubated with mouse blocking buffer on ice for 10 min, followed by staining with the following antibodies: PE-anti-mouse-CD45 (1:100, BD Pharmingen # 553081), FITC-anti-mouse-CD31 (1:100, BioLegend # 102406) and APC-anti-mouse-c-Kit (1:100, Invitrogen #17-1171-82).

Compensation was performed using UltraComp eBeads™ compensation beads (ThermoFisher #01-2222-42). For gating and analysis, markers were determined positive when signal was above FMO (fluorescence minus one) control and in some cases gated with FMO + isotype controls.

Wang *et al. Stem Cell Research & Therapy*   (2024) 15:295

Page 6 of 22

RNA isolation and quantitative PCR with reverse transcription (qPCR) analysis

Total RNA from cells was extracted in TRTzol (Thermo Fisher #15596026) according to manufacturer's instructions. An RNeasy Mini Kit (Qiagen #74104) was used to extract total RNA in EVs. For mRNA qPCR, cDNA was synthesized with 2 ug of RNA using a TaqMan reverse transcription kit (Thermo Fisher #N8080234), followed by qPCR with SYBR Green Master Mix (Thermo Fisher #A25742) to measure expression level of PTEN (for human and mouse; forward primer: 5′-CATGTTGCA GCAATTCACTG-3′, reverse primer: 5′-CTTGTGAAA CAACAGTGCCA-3′). Expression of human β-ACTIN was used as internal control for human cells (forward primer: 5′-TCCTCTCCCAAGTCCACACAGG-3′, reverse primer: 5′-GGGCACGAAGGCTCATCATTC-3′), and expression of mouse β-actin was used as internal control for mouse cells (forward primer: 5′-CGG CCAGGTCATCACTATTGGCAAC-3′, reverse primer: 5′-CCACAGGATTCCATACCCAAGAAG-3′).   For miRNA qPCR, cDNA was synthesized using miRCURY LNA RT kit (Qiagen #339340), and expression levels of *miR-23a-3p* (for both of human and mouse cells; primers purchased from Qiagen #YP00204772), *miR-191-5p* (primers purchased from Qiagen #YP00204306), *miR-532-5p* (primers purchased from Qiagen #YP00204221), RNU48 (reference control for miRNA qPCR of human cells; primers purchased from Qiagen #YP00203903), and snoRNA202 (reference control for miRNA qPCR of mouse cells; primers purchased from Qiagen #YCP2163966) were assessed with miRCURY LNA SYBR Green PCR Kit (Qiagen #339345), following supplier recommended protocols. Relative quantification was performed using the $2^{-\Delta\Delta CT}$ method.

Mice

The work has been reported in line with the ARRIVE guidelines 2.0.

All animal experiments were performed in accordance with approved protocol by the Institutional Animal Care and Use Committee (IACUC) of Shenzhen Institutes of Advanced Technology (SIAT) of the Chinese Academy of Science (CAS). Pregnant female C57BL/6 mice were purchased and shipped from BesTest (Zhuhai, China) to the animal center of SIAT of CAS, and were maintained under standard condition (24–26 °C, relative humidity of 50–70%) with free access to sterilized water and laboratory rodent food. For each experiment, neonatal animals from two to three liters were pooled and assigned to experimental or control groups randomly at birth, ensuring a random mix of sex. Pups were fed by foster dams in a climate-controlled room (24–26 °C, relative humidity of 50–70%) housed under a 12-h dark/light cycle and allowed free access to water and food. We rotated nursing dams between the normoxia and hyperoxia groups every 24 h to avoid oxygen toxicity and associated confounding factors. Oxygen concentration, body weight, evidence of disease, and mortality were monitored daily. Pups with a rapid weight loss of 15% or greater or labored breathing were euthanized. All pups were euthanized by chemical overdose via intraperitoneal injection of pentobarbital (200 mg/kg) and the lungs were harvested for further analysis.

BPD model was induced by continuously exposing C57BL/6 mouse pups to hyperoxia (HYX; 95% O_2 for the first 3 days and changed to 70% O_2 on day 4 till the endpoint) for 14 days. Foster dams were swapped daily between HYX-exposed groups and NOX-exposed groups to prevent injury to the adult mice.

For the clodronate treatment, clodronate liposomes (CLO-lipo; Liposoma BV #C-005) or control PBS liposomes (PBS-lipo; Liposoma BV #P-005) were administered at a dose of 10 uL/g every 3 days starting on day 2, by facial vein injection on day 2 and intraperitoneal injection for the remaining treatments. Lungs were harvested on day 14 and fixed in formalin, and then embedded in paraffin.

AntagomiR-23a-3p or NC (antagomiR-NC) were administered by intraperitoneal injection at a dose of 25 mg/kg every 3 days starting on day 1. Lungs were harvested on day 14. For histology analysis, lungs were fixed in formalin, and then embedded in paraffin. To quantify c-Kit$^+$ EPCs, or to isolate F4/80$^+$ macrophages or CD31$^+$ endothelial cells, harvested lungs were perfused with 5 mL ice-cold PBS supplemented with 1% heparin and digested with mouse lung dissociation kit (Miltenyi #130-095-927) according to manufacturer's instructions. Digested cells were then passed sequentially through 70 μm and 40 μm before density gradient centrifugation using Lymphoprep (STEMCELL Technologies). Single cell suspensions of the mononuclear cell layer were then collected and proceeded with either flow cytometry analysis for c-Kit$^+$ EPC quantification, or isolation of F4/80$^+$ macrophages or CD31$^+$ endothelial cells by using anti-mouse F4/80 Microbeads (Miltenyi Biotec), or anti-mouse CD31 Microbeads (Miltenyi Biotec), respectively, according to the manufacturer's instructions.

mmu-antagomiR-23a-3p (5′-GGAAAUCCCUGGCAA UGUGAU-3′).

Histology

Paraffin-embedded mouse lung sections were stained with H&E to examine tissue morphology and for MLI analysis. Immunohistochemistry (IHC) was performed to assess capillary density in lung sections using vWF (1:5000, Dako #A0082), and staining results were

Wang *et al. Stem Cell Research & Therapy*　　(2024) 15:295

Page 7 of 22

expressed as number of capillary (blood vessels less than 50 μm in diameter) normalized to tissue area (images taken at a ×200 magnification and imageJ was used to quantify tissue area). For IHC of pten expression, lung tissue sections were incubated using anti-pten antibody (1:100, CST #9559).

For immunofluorescence staining, lung tissue sections were incubated using the following primary antibodies: anti-F4/80 antibody (1:200, CST #70076), anti-c-Kit antibody (1:400, CST #7074), and anti-CD31 antibody (1:100, R&D #AF3628) overnight at 4 °C, followed by incubation with combinations of fluorescently tagged secondary antibodies (all used at a concentration of 1:1000, Invitrogen) for 2 h in the dark. Sections were then covered with DAPI (Beyotime, #P0131-25 ml) and allowed to cure in the dark at RT for at least 24 h. Quantifications of F4/80$^+$ macrophages and CD31$^+$c-Kit$^+$ EPCs were performed by counting the number of cells per field of view under confocal microscopy. In each experimental animal at least 5 fields in one section were studied at a 400×magnification.

Two independent researchers blinded to the experimental groups performed the analysis.

EV miRNA library preparation, sequencing, and analysis
The EVs isolated from NOX MDMs (n=3), HYX MDMs (n=3), and TA-M (n=3) were lysed and total RNAs were extracted using RNeasy Mini Kit (QIAEN #74104) according to the manufacturer's protocol. The total RNA was purified by electrophoretic separation (15% polyacrylamide gel), and small RNA regions that corresponded to the 15–40 nt bands were recovered. After gel purification, the 5-adenylated, and 3-blocked adaptor were ligated to the 3′ end of the small RNA fragment. Unique molecular identifier (UMI, for direct molecular counting) labeled adaptor (8–10 nt sequences) was ligated to 5′ end, and the unligated adaptor was digested. Next, Purified RNAs were reverse-transcribed to cDNA with UMI labeled primer, followed by second size selection operation for 103–115 bp fragments from the gel. After gel purification, the PCR yield was quantified by Qubit (Invitrogen, # Q33216) and single-stranded cyclized products were produced (ssDNA circle) to generate final miRNA library. DNA nanoballs (DNBs) were further generated with the ssDNA circle by rolling circle replication (RCR) to enlarge the fluorescent signals at the sequencing process and were sequenced using the DNB-SEQ-G400 (MGISEQ-2000) platform.

After sequencing, the raw reads were filtered and trimmed according to SOAPnuke [31] (removed tags with 5' primer contaminants; remove tags without 3' primer; removed tags without insertion; removed tags

with poly A; removed tags shorter than 18nt). After filtering, the trimmed reads were mapped to the reference genome using Bowtie [32]. miRNAs were quantified by counting absolute numbers of molecules using UMI. Differential abundance of miRNAs was assessed with DESeq. Fold changes and FDR adjusted-*p* values were calculated and used to identify miRNAs significantly differentially expressed between groups.

miRNA sequencing data have been deposited into the CNGB Sequence Archive (CNSA) [33] of China National GeneBank Database (CNGBdb) [34] with accession number CNP 0005647.

miRNA target prediction was performed using TargetScan and miRDB.

Identification of potential miRNA regulators for EPC maintenance
We firstly identified candidate miRNA regulators that were both enriched in EV^{HYX} and EV^{TA-M} by comparing the following miRNAs profiles: EV^{HYX} versus EV^{NOX}; and EV^{TA-M} versus EV^{NOX} (screening criteria: FDR adjusted *p*-value < 0.01, fold-change > 2). The overlapping hits were selected and further ranked based on score calculated using the formula: score = − log (FDR-adjusted *p*-value) × log (fold-change).

Statistical analysis
All results are shown as the mean ± standard deviation (SD) of values. Statistical analyses were performed using GraphPad Prism version 8 (San Diego, CA). A two-tailed unpaired Student's t-test was used for comparison between two groups, and one-way ANOVA were performed for comparisons of data with more than two groups followed by Sidak's correction for multiple comparisons. *P* < 0.05 was considered statistically significant.

Results
Macrophage infiltration leads to c-Kit$^+$ EPC loss in mouse BPD lungs
To evaluate the cell-specific effects of neonatal hyperoxia in vivo, we firstly exposed newborn mice to 14 days (P1-14) of hyperoxic injury, and harvested lungs on day 10 and 14 (Fig. 1A) to assess the impact of neonatal hyperoxia on lung macrophages and c-Kit$^+$ EPCs. As others have previously shown, our analysis also confirmed increased infiltration of macrophages with accompanying loss of EPCs in lungs after prolonged hyperoxia challenge [5, 35], as evidenced by expanded number of F4/80$^+$ population (Fig. 1B, C; Fig. S1A) and significant reduction of CD31$^+$c-KIT$^+$ population (Fig. 1D, E; Fig. S1B). Additionally, the number of F4/80$^+$ macrophages was negatively correlated with number of c-Kit$^+$ EPCs in BPD lungs (Fig. 1F).

Wang *et al. Stem Cell Research & Therapy*   (2024) 15:295

Page 8 of 22

We next utilized clodronate-liposomes (CLO-lipo)—a well-established agent for macrophage depletion, to determine if EPC depletion in BPD lungs could be an effect of macrophage infiltration. The newborn mice, while exposed to hyperoxia, were then randomized to receive treatment either with control-liposomes (PBS-lipo), or CLO-lipo (both PBS-lipo and CLO-lipo were delivered at 10uL/g every 3 days, starting on day 2; workflow shown in Fig. 1G). Immunostainings at P14 revealed that CLO-lipo treatment significantly reduced infiltrating macrophages (Fig. 1H; Fig. S2A), while concomitantly increasing c-Kit$^+$ EPC population relative to those of PBS-lipo-treated group following hyperoxia insult (Fig. 1I, J). In addition, simplified alveoli caused by hyperoxic injury—as shown by increased mean linear intercept (MLI), had been modestly declined by CLO-lipo administration (Fig. S2B). Together, these data suggest that persistent EPC loss following neonatal hyperoxia is at least partially induced by increased macrophage infiltration.

Hyperoxic macrophages decrease human CD34$^+$ EPCs and impair endothelial function of differentiated progeny via EV transmission

To further verify a role for hyperoxic macrophages in hampering human EPC maintenance, we first isolated primary macrophages from tracheal aspirates of human preterm infants requiring mechanical ventilation and oxygen supplementation (TA-M), or exposed human neonatal monocyte-derived macrophages (MDMs; polarized from human CB monocytes [29]) either to hyperoxia (HYX MDMs) or normoxia (NOX MDMs). We then further collected their conditioned media (CM) to add to CB-derived endothelial cell mixtures—which were composed of CD34$^+$ EPCs and mature CD34$^-$ endothelial cells (Fig. 2A). Cultures stimulated with TA-M conditioned medium (CM^{TA-M}) and hyperoxia-exposed MDM medium (CM^{HYX}) had significantly decreased percentages of CD34$^+$ EPCs compared with those stimulated with normoxia-treated MDM medium (CM^{NOX}) over a period of 4 days (Fig. 2B, C). Growth and viability monitoring of CD34$^+$ EPCs at day 4 also revealed significant reduction in proliferation and increased late apoptosis in CM^{TA-M}-treated and CM^{HYX}-treated cultures relative to those of CM^{NOX} control group (Fig. 2D–G). Together, these findings are consistent with the notion that macrophages contribute to EPC loss after hyperoxia insult, and that outcomes of CD34$^+$ EPCs following CM^{HYX} treatment resemble the effects seen in CM^{TA-M}-treated group, indicating use of hyperoxia-exposed human MDM could closely mimic the primary macrophages isolated from a BPD environment.

To assess the paracrine factors released by hyperoxic macrophages that could suppress CD34$^+$ EPC maintenance and determine whether this suppressive modulation might be associated with EV transfer, CD34$^+$ EPCs were isolated immunomagnetically (thereby removing CD34$^-$ mature endothelial cells) and used to initiate cultures treated with whole CM, EV fraction, or EV-depleted CM fraction of TA-M or HYX MDMs (workflow shown in Fig. 3A). Culture received whole CM of NOX MDMs (CM^{NOX}) served as a control because it had previously been shown to give results on CD34$^+$ EPC population comparable to those of untreated culture (Fig. S3). Administration of EVs secreted either from HYX MDMs (EV^{HYX}) or TA-M (EV^{TA-M}) significantly restricted the percentage and number of CD34$^+$ EPCs, and downregulated CD34 expression at primary harvest following 1-week ex vivo culture (Fig. 3B–E). These effects were

(See figure on next page.)

Fig. 1 Infiltrating macrophages contribute to persistent c-Kit$^+$ EPC loss in lungs of newborn mice exposed to prolonged hyperoxia. **A** Experimental scheme for prolonged hyperoxia (HYX) treatment of newborn mice and harvested at P10, or P14 for analysis. n = 6–7 mice for each experimental group. **B** Quantification of macrophages in P10 (upper panel), and P14 (bottom panel) lung sections evaluated with immunofluorescence (F4/80 staining) and quantified as number of F4/80$^+$ cells per field of view. **C** Representative immunofluorescence images of F4/80$^+$ macrophages in P14 mouse lung sections (F4/80, red; DAPI nuclear stain, blue). The dashed white box in the upper image (scale bar, 100 µm) indicates the magnified area shown in the bottom image (scale bar, 50 µm). White arrows mark F4/80$^+$ macrophages. **D** Number of c-Kit$^+$ EPCs in P10 (upper panel), and P14 (bottom panel) lung sections assessed by immunofluorescence (CD31 and c-Kit staining) and quantified as number of CD31$^+$c-Kit$^+$ cells per field of view. **E** Representative immunofluorescence images of c-Kit$^+$ EPCs in P14 mouse lung sections following hyperoxia insult for 14 consecutive days (CD31, green; c-Kit, red; DAPI nuclear stain, blue). The dashed white box in the upper image (scale bar, 100 µm) indicates the magnified area shown in the bottom image (scale bar, 50 µm). White arrows mark c-Kit$^+$ EPCs. **F** Spearman correlation between number of F4/80$^+$ macrophages and c-Kit$^+$ EPCs per field of view in P14 mouse lung sections. Pearson correlation coefficient (r) and p-value are shown. **G** Strategy for examining the impact of macrophage depletion (using clodronate-liposomes (CLO-lipo)) on number of c-Kit$^+$ EPCs in P14 mouse lungs after hyperoxic exposure. **H**–**I** Immunofluorescence analysis to quantify (H) F4/80$^+$ macrophages, and (I) c-Kit$^+$ EPCs in P14 lung sections of hyperoxia-exposed neonatal mice treated with PBS-liposomes (PBS-lipo), or CLO-lipo. **J** Representative immunofluorescence images of c-Kit$^+$ EPCs in P14 lung sections of hyperoxia-exposed mouse after treatment with PBS-lipo, or CLO-lipo (CD31, green; c-Kit, red; DAPI nuclear stain, blue; scale bar, 50 µm). White arrows mark c-Kit$^+$ EPCs. For **G**–**I**, individual mice are shown for each group (n = 7 for PBS-lipo^{NOX}, n = 7 for CLO-lipo^{NOX}, n = 9 for PBS-lipo^{HYX} and n = 8 for CLO-lipo^{HYX}). Groups were compared using Student t test for **B** and **D**, and with one-way ANOVA for **H** and **I** corrected by Sidak's test for multiple comparisons. Error bars represent the SD
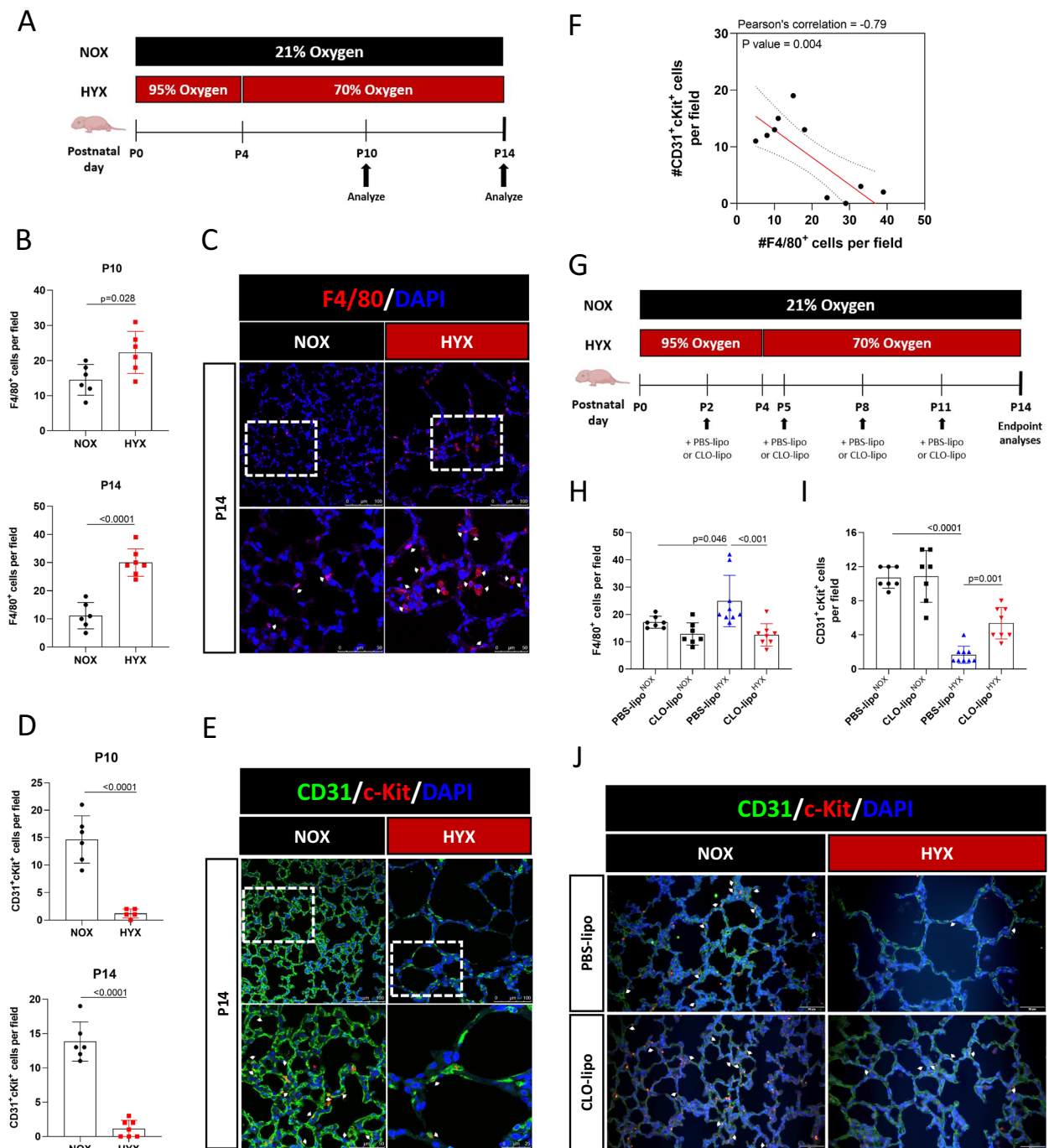
Fig. 1 (See legend on previous page.)

specifically due to EVs, as treatment of EV-depleted CM fraction either from HYX MDMs (EV-depleted^{HYX}) or TA-M (EV-depleted^{TA-M}) did not display similar inhibitory actions on CD34$^+$ EPCs. Furthermore, examination of the progeny produced from CM^{NOX}-treated cultures as of 1 week later showed majority of cells exhibited a rounded shape, similar to those observed in EV-depleted

CM-treated cultures. This contrasted with the elongated endothelial morphology expected for differentiated endothelial progeny [36] found in the EV^{HYX}-treated and EV^{TA-M}-treated cultures, and their respective CM-treated groups (Fig. 3F), thus further supporting the finding that hyperoxic macrophages inhibit CD34$^+$ EPC maintenance via EV transmission.

To evaluate the biological consequences of EV uptake by CD34$^+$ EPCs, we next replated cells from the initial cultures and perform endothelial functional assays on differentiated progeny at secondary harvest (Fig. 3A). Both of differentiated progeny derived from EV^{HYX}-treated and EV^{TA-M}-treated groups exhibited clear decreases in the capacity of migration (Fig. 4A, B) and formation of vascular networks (Fig. 4C, D), thus recapitulating the suppressive effects on endothelial function also seen in those derived of respective CM-treated groups. Collectively, these data suggest that suppression of CD34$^+$ EPC maintenance and endothelial function of their progeny by hyperoxic macrophages is attributed to EV transmission.

miR-23a-3p is enriched in hyperoxic macrophage-derived EVs

Morphological assessment of isolated EV produced from NOX MDMs, HYX MDMs, or TA-M by transmission electron microscopy revealed the typical and expected cup-shaped morphology (Fig. S4A), with an average diameter ranging between 100 and 200 nm (Fig. S4B) quantified by nanoparticle tracking analysis (NTA), in accordance with the range expected for small EVs [23]. Western blotting also confirmed that isolated EVs expressed classical EV markers CD81, CD63, Alix, and negative for cytoplasmic marker GM130 (Fig. S4C). Subsequent confocal microscopy analysis confirmed the internalization of EVs into CD34$^+$ EPCs by direct visualization of colocalization of Dio-labelled EVs with RAB7$^+$ late endosomes in the cytoplasm of CD34$^+$ EPCs (Fig. S4D).

Several miRNAs have been identified to be critical regulators involved in the pathogenesis of BPD [37], and macrophage-derived EVs capable of exerting functional roles in recipient cells through miRNA-enriched bioactive cargo have also been documented in various lung diseases [21, 25]. To identify the potential miRNA regulators in enacting inhibitory effects on CD34$^+$ EPC maintenance, we performed the microRNA transcriptome

to screen for miRNAs both enriched in EV^{HYX} and EV^{TA-M} by comparing the following miRNAs profiles: EV^{HYX} versus EV^{NOX}; and EV^{TA-M} versus EV^{NOX}. We identified 8 miRNAs that were significantly upregulated by more than twofold in both of EV^{HYX} and EV^{TA-M} relative to respective expressions in EV^{NOX} (with the screening criteria of FDR adjusted p-value < 0.01 and fold-change > 2). These 8 overlapping miRNA candidates were further ranked based on adjusted p-value and fold change (Supplementary Table 2), with the top 3 miRNA candidates identified as miR-191-5p, miR-532-5p, and miR-23a-3p (Fig. 5A, B). As an initial investigation into the impact of the top 3 miRNAs on CD34$^+$ EPC maintenance, we directly transfected CD34$^+$ EPCs with miR-191-5p/miR-532-5p/miR-23a-3p mimics or NC-mimic (negative control), and cultured transfected cells ex vivo for 4 days followed by flow cytometry analysis. miR-191-5p-treated and miR-23a-3p-treated cultures had significantly reduced percentages of CD34$^+$ EPCs and downregulated CD34 expression compared with those of miR-NC control (Fig. 5C). Morphological examination of the progeny produced from miR-191-5p -transfected CD34$^+$ EPCs exhibited a rounded shape, whereas progeny in miR-23a-3p-transfected culture displayed an elongated endothelial morphology (Fig. 5D), which more closely resembles those observed for differentiated progeny in EV^{HYX}-treated and EV^{TA-M}-treated cultures (Fig. 3F). qPCR analysis on expressions of *miR-191-5p*, *miR-532-5p*, and *miR-23a-3p* (Fig. 5E; Fig. S5 and S6) revealed that expressions of *miR-23a-3p* were significantly increased by more than 11-fold in TA-M and trended to enhance by more than twofold in HYX MDMs than that of NOX MDMs. Moreover, similar to the expression profiles in macrophages, only *miR-23a-3p* exhibited markedly higher expression in both of EV^{TA-M} (increased by almost ninefold) and EV^{HYX} (upregulated by fourfold) than that in EV^{NOX} control (Fig. 5F; Fig. S5 and S6). Therefore, *miR-23a-3p* was selected for further study.

(See figure on next page.)
Fig. 2 Human hyperoxic macrophages promote CD34$^+$ EPC loss during ex vivo culture. **A** Schematic depicting the experimental design of the in vitro culture workflow to determine the impact of human hyperoxic macrophages on human CD34$^+$ EPC maintenance. **B**, **C** Representative flow cytometry plots in panel **B** for gating of CD34$^+$ EPCs (characterized by CD31$^+$CD34$^+$) within live cell population at day 4 after treatment with condition medium (CM). CM were collected from cultures of normoxia-exposed CB monocyte-derived macrophages (CM^{NOX}), hyperoxia-treated CB monocyte-derived macrophages (CM^{HYX}), or primary macrophages isolated from tracheal aspirates of human preterm infants requiring mechanical ventilation and oxygen supplementation (CM^{TA-M}). Culture received CM^{NOX} served as control. Statistical comparisons of the frequency of CD34$^+$ EPCs following indicated treatments for 2 or 4 days are shown in panel **C**. n = 3 per group. **D**–**E** Representative flow cytometry plots in panel **D** and frequency of proliferating Ki67$^+$ cells in panel **E** within CD34$^+$ EPC fraction after treatment with CM^{NOX}, CM^{HYX}, or CM^{TA-M} for 4 days. Culture received CM^{NOX} served as control. n = 3 per group. **F**–**G** Representative flow cytometry plots in panel **F** and fraction of CD34$^+$ EPCs undergoing late apoptosis in panel **G**; characterized by annexin V$^+$PI$^+$) after treatment with CM^{NOX}, CM^{HYX}, or CM^{TA-M} for 4 days. Culture received CM^{NOX} served as control. n = 3 per group. Groups were compared using one-way ANOVA corrected by Sidak's test for multiple comparisons. Error bars represent the SD
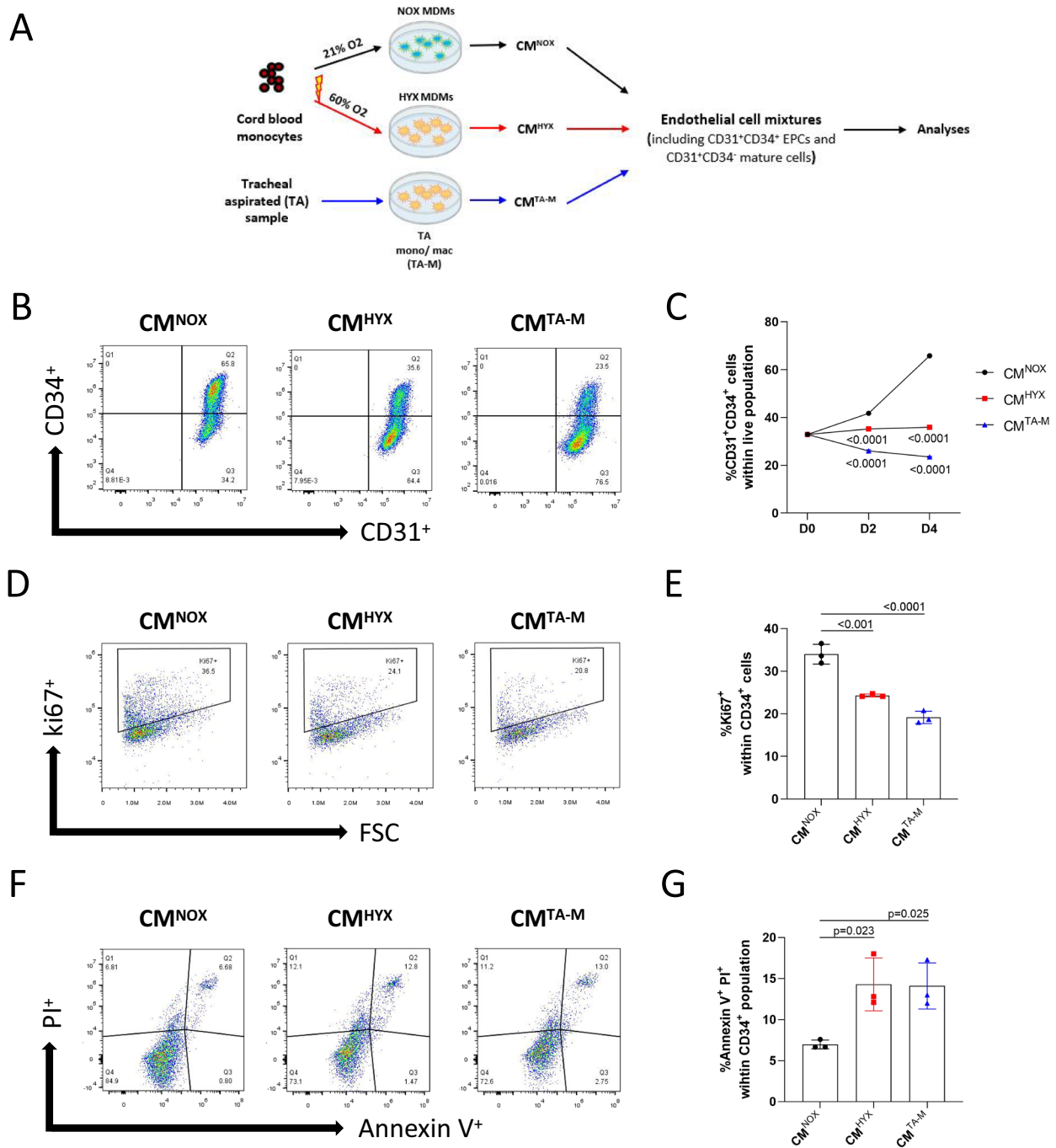
Fig. 2 (See legend on previous page.)

Targets of *miR-23a-3p* were predicted using two publicly available prediction algorithms—TargetScan and miRDB, and 54 common targets were identified (Fig. S7A). Among them, we chose to further validate *PTEN*, which has been reported to be a target

of *miR-23a-3p* [38, 39] and associated with stem cell/ progenitor maintenance [40, 41]. qPCR assessment of CD34$^+$ EPCs transfected with miR-23a-3p mimic confirmed that *PTEN* expression was significantly reduced compared to that of miR-NC control (Fig. S7B).
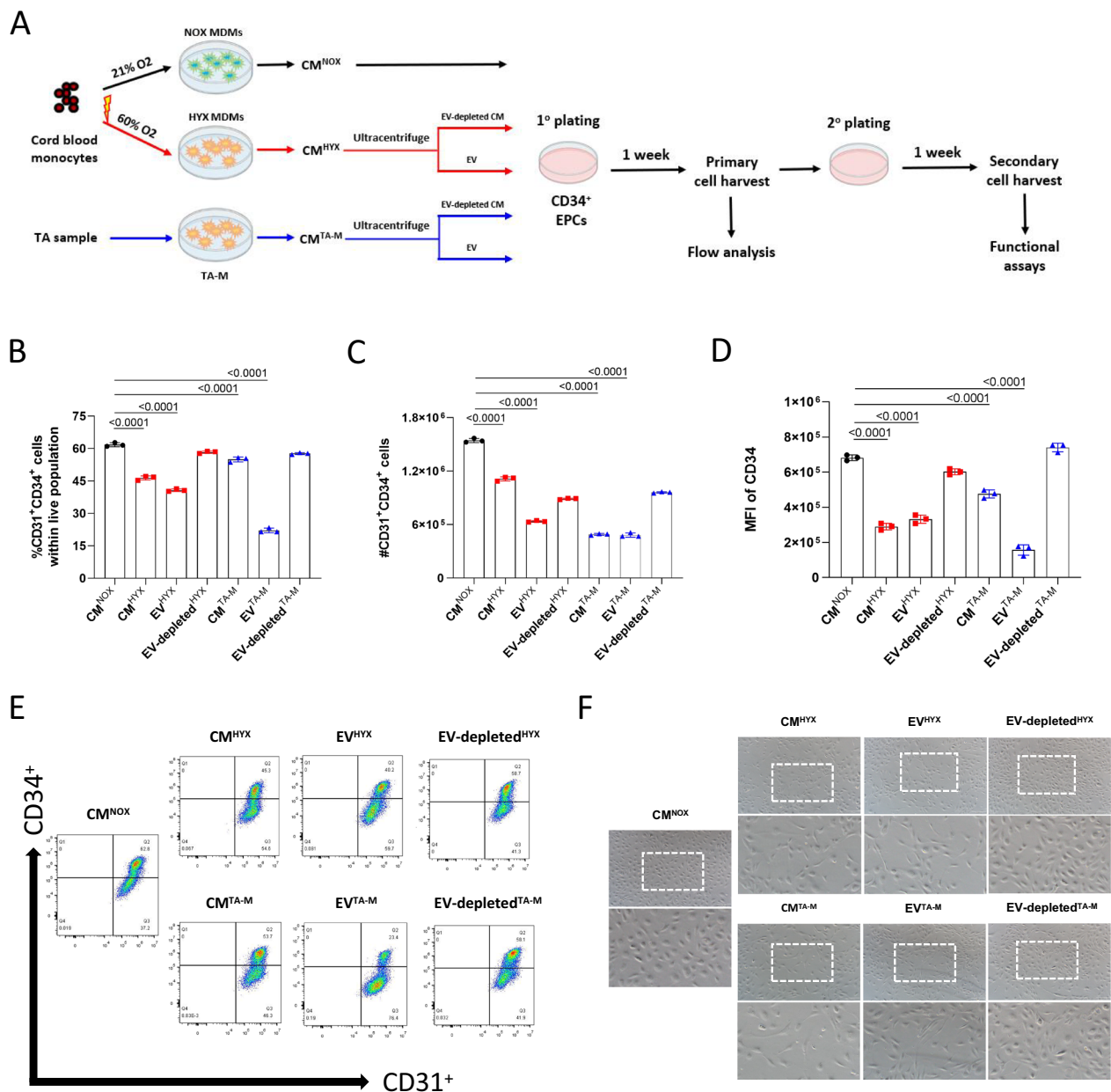
Fig. 3 Human hyperoxic macrophages restrict CD34+ EPC expansion through extracellular vesicles (EVs). **A** Strategy for assessing the paracrine factors released by hyperoxic macrophages that could inhibit CD34+ EPC maintenance and endothelial function of the differentiated progeny. **B**, **D** Quantification by percentage **B**, number **C**, and mean fluorescence intensity (MFI, D) of CD34+ fraction within the live progeny of purified CD34+ EPC cultures following 1-week treatment with CM, EV-depleted fraction, or EVs derived from HYX MDMs (CM^HYX, EV-depleted^HYX, or EV^HYX, respectively), or TA-M (CM^TA-M, EV-depleted^TA-M, or EV^TA-M, respectively). Purified CD34+ EPC culture received whole CM of NOX MDMs (CM^NOX) served as control. n = 3 per group. **E** Representative flow cytometry plots for gating of CD34+ EPCs (characterized by CD31+CD34+) within live cell population at 1-week with the indicated treatments. **F** Representative images of progeny derived from purified CD34+ EPC cultures taken at following 1-week treatment with CM, EV-depleted fraction, or EVs of indicated macrophage cultures. Scale bar: 200 μm. The magnified regions are marked by dashed white boxes, and presented beneath the original images. Groups were compared using one-way ANOVA corrected by Sidak's test for multiple comparisons. Error bars represent the SD
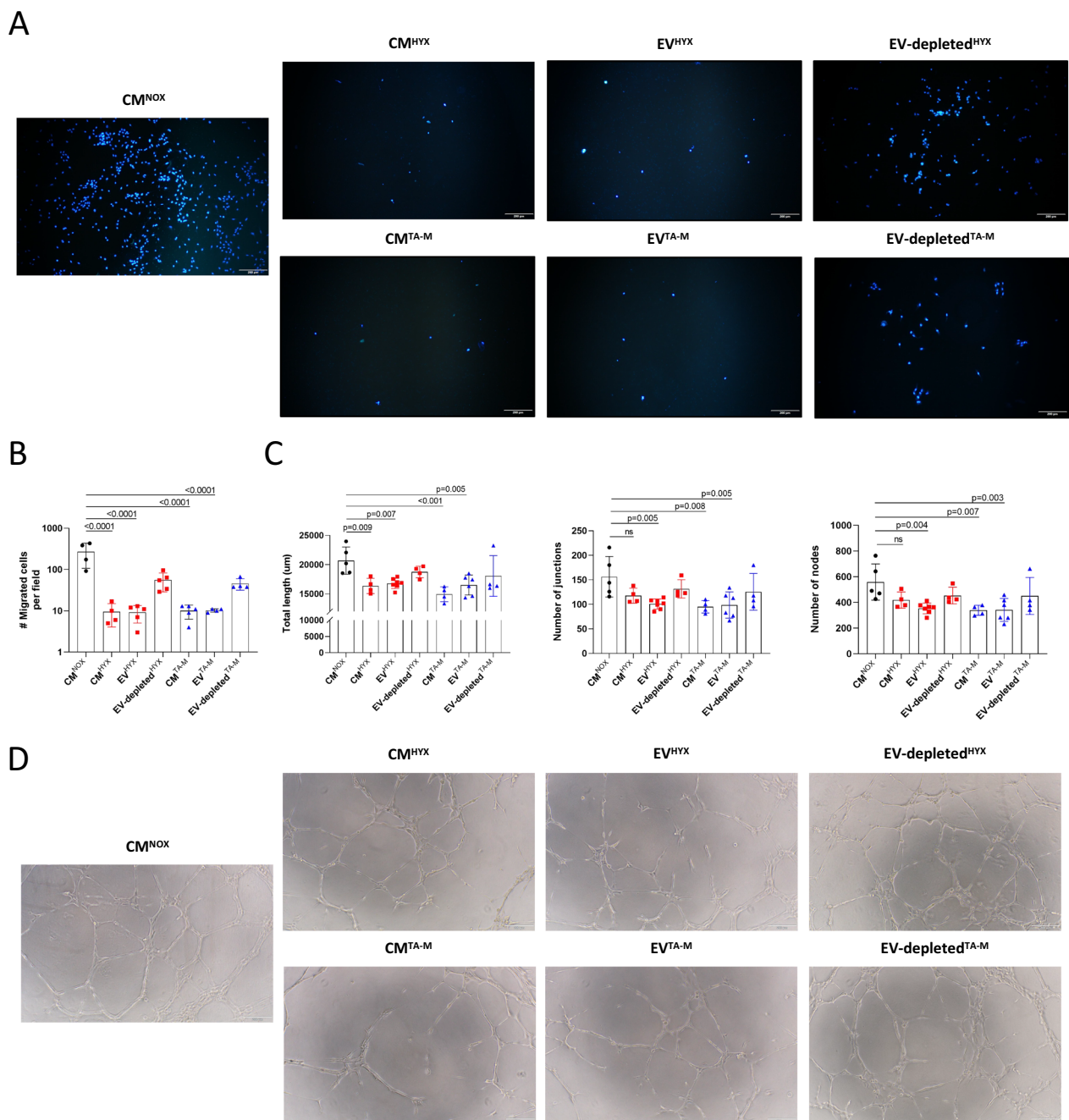
Fig. 4 EVs from hyperoxic macrophages impair endothelial capacity of differentiated CD34$^+$ EPC progeny. **A**, **B** Transwell migration assays were performed to assess the migration potential of CD34$^+$ EPC differentiated progeny after 2-week treatment with CM, EV-depleted fraction, or EVs from HYX MDMs (CM^{HYX}, EV-depleted^{HYX}, or EV^{HYX}, respectively) or TA-M (CM^{TA-M}, EV-depleted^{TA-M}, or EV^{TA-M}, respectively). Purified CD34$^+$ EPC culture following 2-week treatment with whole CM of NOX MDMs (CM^{NOX}) served as control. Representative images of migrated cells are shown in panel (A), and statistical comparisons of the migrated cell number are shown in panel **B**. n = 4–5 per group. **C**, **D** Quantification of tube forming ability of differentiated CD34$^+$ EPC progeny following 2-week culture in conditions indicated in columns in **C**, using tube formation assay to evaluate tube length (left panel), number of junctions (middle panel), and number of nodes (right panel). Representative images of tube formation assay on treated-EPC progeny are shown in **D**. Differentiated progeny of CM^{NOX} group served as control. n = 5–7 per group. All scale bars denote 200 μm. Groups were compared using one-way ANOVA corrected by Sidak's test for multiple comparisons. Error bars represent the SD

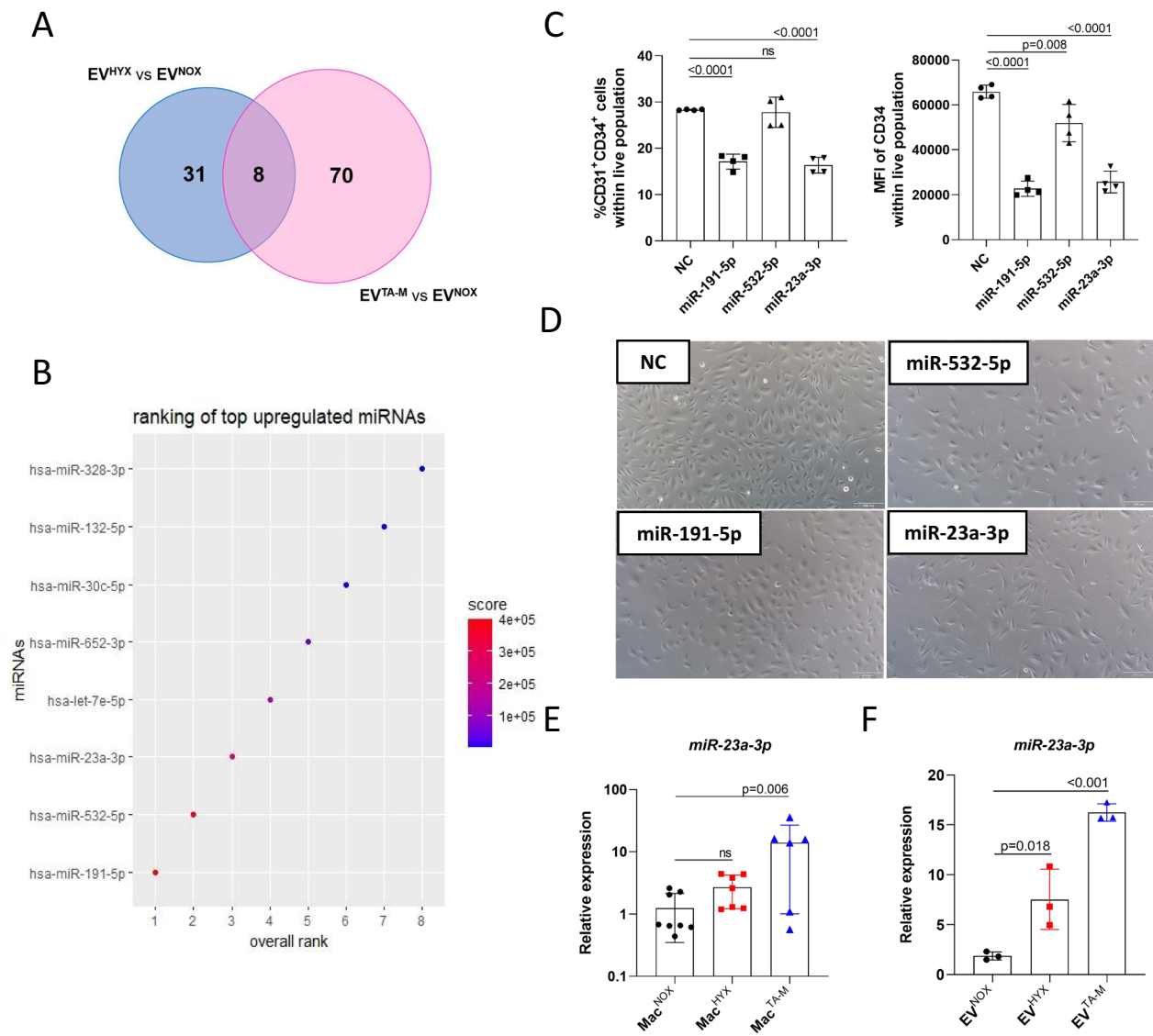Wang *et al. Stem Cell Research & Therapy* (2024) 15:295

Page 14 of 22

Fig. 5 *miR-23a-3p* is enriched in EVs of hyperoxic macrophages and related to EPC loss. **A** Number of miRNA genes simultaneously elevated in both of EV^{HYX} and EV^{TA-M} compared to those in EV^{NOX} control (screening criteria: false discovery rate [FDR]–adjusted $P < 0.01$, fold change > 2). **B** Ranking of overlapping miRNA candidates from **A** that were predicted to be upregulated in both of EV^{HYX} and EV^{TAM} compared to those of EV^{NOX}. Ranking is based on FDR-adjusted P-value and fold change, better-ranking candidates have higher scores and lower overall rank. **C** Proportion of CD34$^+$ population and MFI of CD34 expression within live progeny of CD34$^+$ EPCs after transfection with either miR-191-5p/miR-532-5p/ miR-23a-3p mimics or miR-NC (NC, negative control) and culture over a 4-day period. n = 4 per group. **D** Representative images of progeny of CD34$^+$ EPCs after transfection with either miR-191-5p/miR-532-5p/miR-23a-3p mimics or miR-NC and culture over a 4-day period. Scale bar: 200 μm. **E** Relative levels of *miR-23a-3p* in HYX MDMs and TA-M compared to that of NOX MDMs, assessed by qPCR. n = 6–8 per group. **F** Relative levels of *miR-23a-3p* in EV^{HYX} and EV^{TA-M} relative to that of EV^{NOX}, assessed by qPCR. n = 3 per group. Groups were compared using one-way ANOVA corrected by Sidak's test for multiple comparisons. Error bars represent the SD

Elevated *miR-23a-3p* transmitted by EVs induces CD34$^+$ EPC loss and impairs endothelial capacity in the differentiated progeny

To confirm that the observed inhibitory effects on CD34$^+$ EPCs were driven by the *miR-23a-3p* in EVs, we next transfected EV^{NOX} with miR-23a-3p mimic or NC

mimic, followed by treating CD34$^+$ EPCs with these miRNA-loaded EVs (Fig. 6A). qPCR analysis confirmed that the expression level of *miR-23a-3p* was significantly increased in the CD34$^+$ EPCs treated with miR-23a-3p mimic-loaded EV^{NOX} (23a-3p mimic-EV^{NOX}; Fig. S8). Administration of 23a-3p mimic-EV^{NOX} to CD34$^+$ EPCs

Wang *et al. Stem Cell Research & Therapy*   (2024) 15:295

Page 15 of 22

significantly decreased proliferation while simultaneously promoting late apoptosis of CD34^{+} EPCs compared with those of NC-mimic-EV[NOX]-treated cells (Fig. 6B; Fig. S9), thus resulting in a significant reduction of percentage and number of CD34^{+} EPCs in 23a-3p mimic-EV[NOX]-treated group at primary harvest (Fig. 6C). To further investigate on the angiogenic potency of differentiated progeny produced from 23a-3p mimic-EV[NOX]-treated culture, we performed tube formation assay to assess endothelial capacity of vessel formation; transwell assay and wound healing assay to evaluate migration capacity of the endothelial progeny. 23a-3p mimic-EV[NOX] treatment resulted in impaired endothelial function, as reflected by a lower endothelial capability to form vessel structures (Fig. 6D, E) and migrate (Fig. 6F, G for transwell assay; Fig. 6H, I for wound healing assay).

Given that EV-transmitted *miR-23a-3p* inhibited maintenance and functionality of CD34^{+} EPCs, we next asked whether such suppressive effects could be rescued by silencing *miR-23a-3p*. EV[HYX]—wherein expression level of *miR-23a-3p* has been confirmed to be upregulated by fourfold relative to that in EV[NOX] (Fig. 5F), was next transfected EV[HYX] with miR-23a-3p inhibitor to downregulate *miR-23a-3p* expression and treated on CD34^{+} EPCs (Fig. 6A; Figure S8). Silencing the *miR-23a-3p* in EV[HYX] (23a-3p inhibitor-EV[HYX]) abrogated the inhibitory effect of EV[HYX] on CD34^{+} EPC proliferation following 1-week ex vivo culture at primary culture (Fig. 6B), hence improving the retention of CD34^{+} EPCs, both by percentage and number compared with those of NC-inhibitor-EV[HYX]-treated cells (Fig. 6C). 23a-3p inhibitor-EV[HYX]-treated culture had similar degree of late apoptosis in CD34^{+} EPCs compared to NC inhibitor-EV[HYX]-treated control, suggesting that administration of 23a-3p inhibitor-EV[HYX] did not alter this phenotype (Fig. S9). Furthermore, downregulation of *miR-23a-3p* in EV[HYX] was able to partially restore endothelial function of differentiated progeny at secondary harvest, as

demonstrated by significantly increased tube formation (Fig. 6D, E) and migration (Fig. 6F–I) capacity of 23a-3p inhibitor-EV[HYX]-treated progeny relative to those of NC-inhibitor-EV[HYX]-treated cells.

Next we sought to determine whether modifications of *miR-23a-3p* level influence PTEN expression in CD34^{+} EPC progeny. qPCR assessment revealed that *PTEN* expression was significantly downregulated in 23a-3p mimic-EV[NOX]-treated cells compared to that of NC-mimic-EV[NOX]-treated group (Fig. S10A). Hyperoxia exposure further suppressed *PTEN* expression, however, silencing *miR-23a-3p* in EV[HYX] did not reverse this effect (Fig. S10A), likely reflecting that *miR-23a-3p* is not the sole driver downregulating *PTEN* expression. Immunofluorescence microscopy confirmed the suppression of PTEN protein expression in 23a-3p mimic-EV[NOX]-treated and NC-inhibitor-EV[HYX]-treated group compared to that of NC-mimic-EV[NOX]-treated group (Fig. S10B). In contrast to the qPCR result, silencing of *miR-23a-3p* in EV[HYX] was able to restore PTEN expression comparable to that of NC-mimic-EV[NOX]-treated group (Fig. S10B).

Taken together, these data highlight the role that EV-transmitted *miR-23a-3p* plays in modulating the suppressive activities of hyperoxic macrophages on CD34^{+} EPCs.

Inhibition of *miR-23a-3p* improves c-KIT^{+} EPC maintenance, enhances capillary density, and ameliorates simplified alveolarization in mouse BPD lungs

Considering the beneficial effects of silencing *miR-23a-3p* demonstrated in our in vitro studies, we next investigate the therapeutic impact of antagomiR-23a-3p in vivo by administrating antagomiR-23a-3p (injected at 25 mg/kg of body weight) or antagomiR-NC (NC) intraperitoneally to mice subjected to hyperoxic injury (antagomiR-23a-3p[HYX] or NC[HYX]; Fig. 7A). qPCR assessment confirmed that although *miR-23a-3p* expression levels were significantly upregulated in lung F4/80^{+}

(See figure on next page.)

Fig. 6 EV-transmitted *miR-23a-3p* drives CD34^{+} EPC exhaustion. **A** Experimental scheme outlining the treatment of CD34^{+} EPCs with corresponding miRNA mimics/inhibitors-loaded EVs: EV[NOX] were loaded with NC mimic or miR-23a-3p mimic; EV[HYX] were loaded with NC inhibitor or miR-23a inhibitor. **B** Proportion of proliferating Ki67^{+} cells within CD34^{+} population at day 7 following treatment of CD34^{+} EPCs with EVs loaded with corresponding miRNA mimics or inhibitors. n = 3 per group. **C** Frequency (left panel; n = 6–7 per group) and number (right panel; n = 3 per group) of CD34^{+} fraction within live progeny of purified CD34^{+} EPC cultures following 1-week culture in conditions indicated in columns. **D, E** Tube formation assays **D** were performed to evaluate tube length (left panel), number of junctions (middle panel), and number of nodes (right panel) of differentiated progeny of CD34^{+} EPCs after 2-week treatment with loaded-EVs indicated in columns **E**. n = 4–6 per group. **F, G** Transwell migration assays were performed to assess the migration potential of differentiated CD34^{+} EPC progeny following 2-week culture in conditions indicated in columns, and statistical comparisons of the migrated cell number are shown in **F**. Representative images of migrated cells are displayed in **G**. n = 4 per group. **H, I** The migration potential of differentiated CD34^{+} EPC progeny from conditions indicated in columns (**H**), was also measured using the wound closure assay. Statistical comparisons of the percent wound closure are presented in **H**, and representative images of wound closure are shown in **I**. n = 4 per group. Groups were compared using one-way ANOVA corrected by Sidak's test for multiple comparisons. Error bars represent the SD
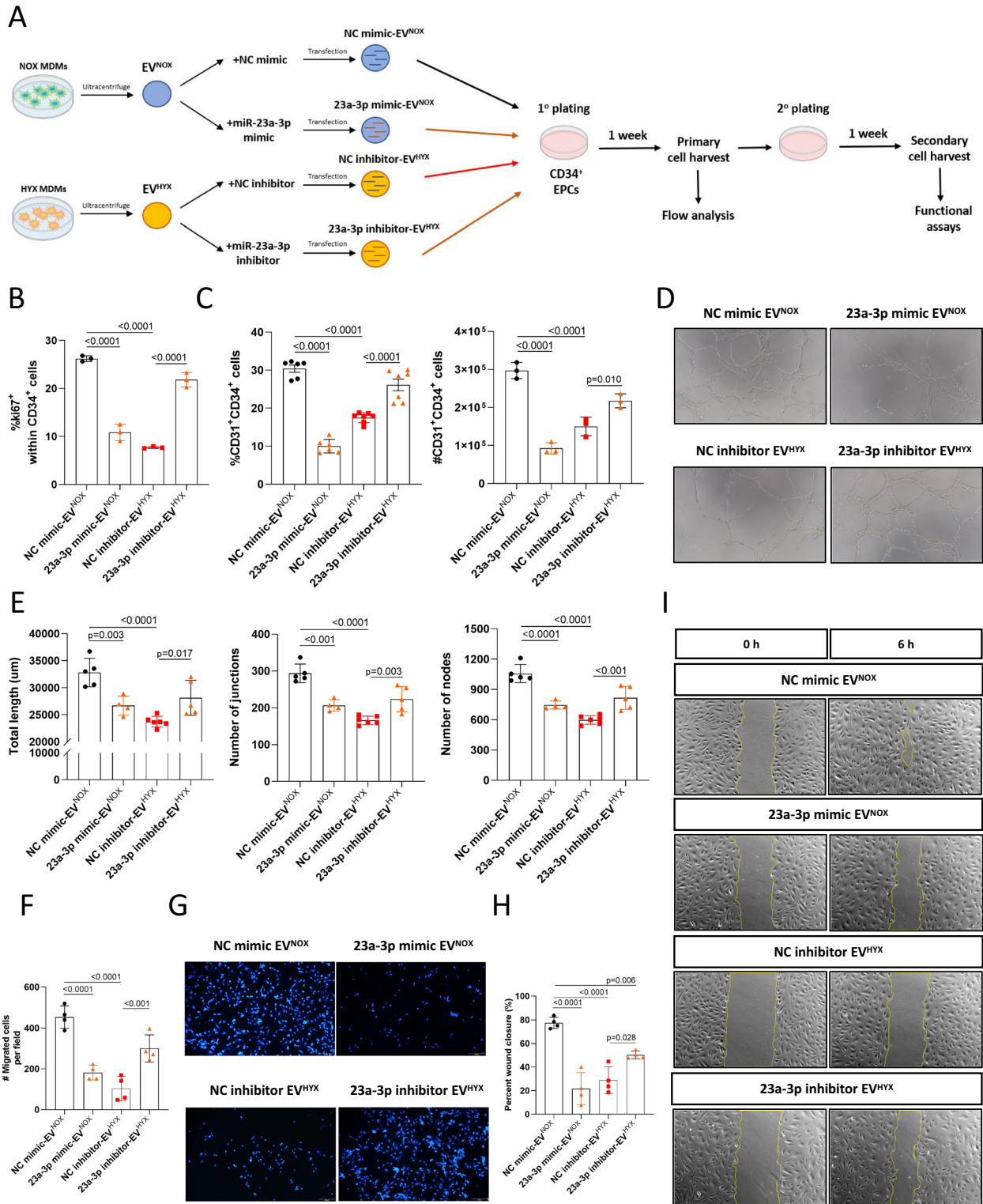
Fig. 6 (See legend on previous page.)

macrophages and CD31$^+$ endothelial populations from mice subjected to hyperoxic injury (Fig. 7B, C), treatment with antagomiR-23a-3p effectively reduced *miR-23a-3p* expression levels in these two populations comparable to those of NC-treated mice in normoxia (NC^{NOX}; Fig. 7B, C). Immunofluorescence staining revealed significantly increased number of c-Kit$^+$ EPCs in lungs of antagomiR-23a-3p-treated mice compared to that in NC-treated mice after hyperoxia insult (Fig. 7D, E). These results were further corroborated by flow cytometry analysis showing significantly higher percentage and number of cKit$^+$ EPCs in lungs of antagomiR-23a-3p^{HYX}-treated mice relative to those of NC^{HYX}-treated group (Fig. 7F). To further explore the potential impact of antagomiR-23a-3p administration on pulmonary capillary density—which is reflective of in vivo functional capacity, we assess von Willebrand factor (vWF) staining in lung sections of P14 mice after hyperoxia treatment. Compared to NC^{NOX}-control mice, hyperoxia exposure resulted in significant reduction of capillary density, whereas antagomiR-23a-3p treatment restored this outcome (Fig. 7G, H)—which was indicative of an ability of antagomiR-23a-3p administration to improve in vivo functional capacity of differentiated EPC progeny. We next went to uncover whether silencing of *miR-23a-3p* in vivo could promote alveolarization. Lung histological analysis showed that NC^{HYX}-treated mice exhibited alveolar simplification, as characterized by an elevated MLI compared to that of NC^{NOX}-treated group. However, treatment of antagomiR-23a-3p ameliorated the hypoalveolarization observed in NC^{HYX}-treated group, which was confirmed by decreasing MLI in antagomiR-23a-3p^{HYX}-treated mice compared to that of NC^{HYX}-treated mice (Fig. 7I, J). Last, we investigated pten expression in lung endothelium of P14 mice following hyperoxia exposure. Administration of antagomiR-23a-3p to BPD mice resulted in improved *pten* expression in lung CD31$^+$ endothelial population (Fig. S11A). In addition, we performed immunostaining to evaluate pten expression in mouse BPD lung sections. We observed that hyperoxia exposure dramatically decreased pten staining in the lung sections—including small vessels, whereas antagomiR-23a-3p treatment reversed this effect and strong pten staining could be detected on small vessels in hyperoxia-exposed lung sections (Fig. S11B).

Collectively, these data demonstrate that antagomiR-23a-3p treatment promotes lung alveolarization in BPD model via improving c-Kit$^+$ EPC maintenance and functional capacity of differentiated EPC progeny.

Discussion

Here, we provide direct evidence that hyperoxic macrophages disrupt EPC maintenance, both in mice and humans. Moreover, we are the first to identify a novel mechanism by which hyperoxic macrophages are able to inhibit EPC maintenance and impair endothelial function of the differentiated progeny, through release of EVs enriched with *miR-23a-3p*. This study further shows that inhibition of *miR-23a-3p* expression in vivo offers an innovative pharmacological strategy to enable EPC maintenance and capillary density to be restored, which results in improved alveolarization in hyperoxia-injured lungs.

The properties of c-Kit$^+$ EPCs have been successfully exploited experimentally in mice to interrogate molecular mechanisms that regulate the maintenance of c-Kit$^+$ EPCs during neonatal vascular development and injury [5, 42]. However, the phenotypic and functional outputs of human EPCs along with the underlying pathologic mechanisms inducing their loss after hyperoxia exposure remain unclear. Previous work demonstrated that c-Kit$^+$ EPC number and proliferation were

(See figure on next page.)

Fig. 7 AntagomiR-23a-3p treatment in BPD model enhances pulmonary c-Kit$^+$ EPC maintenance, capillary density, and lung alveolarization. **A** Schematic of experimental BPD mouse model assessing the impact of silencing *miR-23a-3p* on c-Kit$^+$ EPC maintenance and lung architecture. Briefly, newborn mouse pups were exposed to normoxia (NOX) or hyperoxia (HYX) condition and distributed over two groups for either receiving antagomiR-negative control (NC) or antagomiR-23a-3p (25 mg/kg) every three days. **B** Relative levels of *miR-23a-3p* in isolated lung F4/80$^+$ macrophages, assessed by qPCR. n = 6 per group. **C** qPCR assessment of *miR-23a-3p* in isolated lung CD31$^+$ endothelial cells. n = 6 per group. **D, E** Immunofluorescence staining experiment of c-Kit$^+$ EPCs (CD31 and cKit staining) in P14 lung sections of hyperoxia-exposed mice after treatment with NC, or antagomiR-23a-3p. c-Kit$^+$ EPCs were quantified as number of CD31$^+$c-Kit$^+$ cells per field of view, and statistical comparisons are shown in **E**. Representative immunofluorescence images are shown in (panel **D**; CD31, green; c-Kit, red; DAPI nuclear stain, blue; scale bar, 50 μm). White arrows mark c-Kit$^+$ EPCs. n = 5 mice for each experimental group. **F** Percentage (left panel) and number (right panel) of pulmonary c-Kit$^+$ EPCs within live CD45$^-$ population, assessed by flow cytometry analysis of P14 lungs of hyperoxia-exposed mice after treatment with NC, or antagomiR-23a-3p. n = 5–6 mice for each experimental group. **G, H** Immunostainings (representative figures shown in panel **G**; Scale bar: 100 μm) and quantification of capillary (panel **H**; characterized by vWF-labeled microvessels less than 50um in diameter) in P14 lung sections of hyperoxia-exposed mice after treatment with NC, or antagomiR-23a-3p. n = 4–5 mice for each experimental group. **I, J** Representative images of haematoxylin & eosin staining (H&E staining; panel **I**) to assess alveolar complexity at P14. Scale bar: 100 μm. MLI quantification of alveolarization was determined and shown in panel **J**. n = 4–5 mice for each experimental group. Groups were compared using Student *t* test for **E** and **F**, and with one-way ANOVA for **B**, **C**, **H** and **J** corrected by Sidak's test for multiple comparisons. Error bars represent the SD
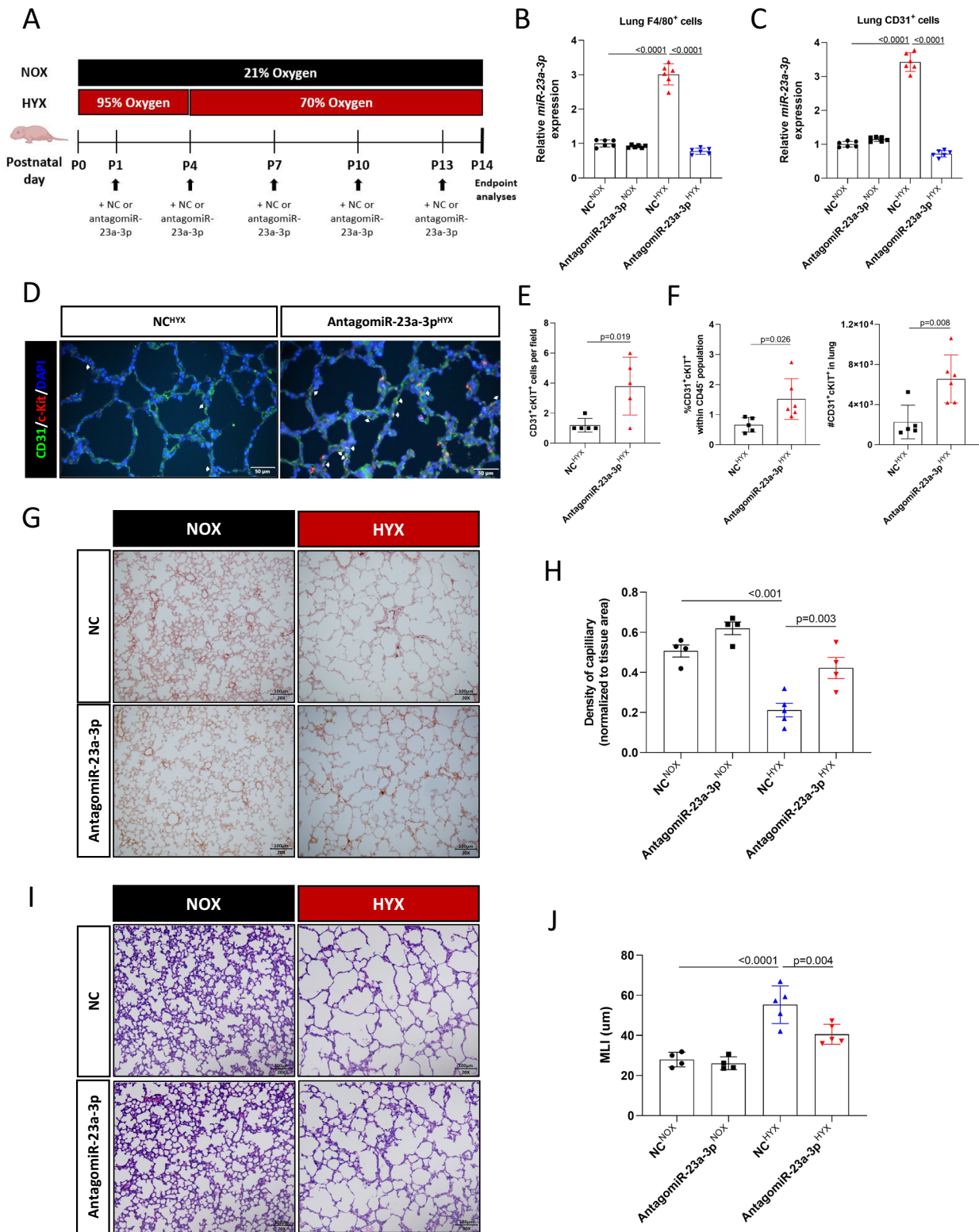
Wang *et al. Stem Cell Research & Therapy*   (2024) 15:295

Page 18 of 22

Fig. 7 (See legend on previous page.)

Wang *et al. Stem Cell Research & Therapy*   (2024) 15:295

Page 19 of 22

all reduced in mouse BPD model [5], consistent with findings in human BPD patients where circulating EPCs were found to be significantly decreased [11, 12]. This deficiency in the capability of proliferation, together with our data indicating that human EPCs and their progeny are functionally impaired to migrate and form new vessels, are reflective of "exhaustion" of human EPCs in BPD, similar to the exhaustion of immune cells observed in chronic infections [43]. Our study demonstrates that hyperoxic macrophages induce human EPC exhaustion through EV-transmitted *miR-23a-3p*, thereby providing potential target for designing clinical therapeutic strategies.

Macrophages are key modulators of inflammatory lung environment in BPD. Evidence of hyperoxia exposure shifting the lung macrophage population toward a pro-inflammatory phenotype has been reported in mouse BPD model and inferred from samples of human BPD patients [18, 44, 45]. Interestingly, when macrophages were depleted in BPD mice using clodronate liposomes in our study—although c-Kit⁺ EPCs were significantly increased, alveolarization were only modestly improved. This slightly contrasts with previous work showing that alveolarization could be significantly enhanced by depleting resident macrophages or infiltrating monocytes/macrophages upon hyperoxia exposure, using AP20187-treated macrophage Fas-induced apoptosis mice (MAFIA model), or ccr2⁻ᐟ⁻ mice, respectively [17]. The variable outcomes in alveolarization following macrophage depletion likely reflect that lung environment consists of a complex orchestration of cells, with important repercussions on lung alveolarization if macrophages are depleted. Therefore, further understanding of the mechanisms with a special focus on paracrine actions by which macrophages affect EPC maintenance instead of simple depletion of macrophage population, would open up avenues for developing new therapies for BPD. Efforts to date have led to the identification of several pro-inflammatory cytokines and chemokines important to BPD progression [18, 45, 46]. However, these potential treatment strategies are currently limited to the preclinical stage, and clear evidence of increased clinical significance remains lacking, thus highlighting the need for a better understating of the pathologic pathways that drive EPC exhaustion to more accurately identify new therapeutic targets for BPD. Here, we found that EVs derived from hyperoxic macrophages can exert intercellular communication to modulate EPC maintenance and functionality. The ability of macrophage-derived EVs to either circulate to distal niche or reside in local environment to carry out their physiological functions has been documented in various diseases, including cancer,

diabetes, and other cardiovascular and metabolic disorders [21, 47]. For example, Wang et al. [47] have shown that macrophage-derived EVs impair endothelial cell function and hinder wound healing in diabetic wounds. Intestinal macrophage-derived EVs affect intestinal stem cells and are essential for regenerative response of intestine post-irradiation [22]. Furthermore, the ability of macrophage-derived EVs to travel to distal sites and promote metastasis has been well-documented in many cancers [21]. Therefore, EV shuttling from hyperoxic macrophages may be able to regulate EPCs in the neonatal lung tissue or in the circulation, making this a candidate mechanism that warrants further investigation.

miR-23a-3p has previously been reported to be upregulated in studies from cancer, diabetes, aging, and rickettsial infection fields [48–51], and that the pathologies were possibly associated with dysregulated angiogenesis [51, 52]. For example, Zhou et al. recently demonstrated that *miR-23a-3p* can be transmitted by endothelial EVs to disrupt microvascular endothelial barrier following rickettsial infection [51]. By contrast, Oikawa et al. [53] did not find any abnormalities on angiogenesis following vascular endothelial cell-specific knockout of *microRNA-23* cluster. More recently, Li et al. discovered that *miR-23a-3p* overexpression promotes cell viability of pulmonary vascular endothelial cells after exposure to cigarette smoke extract, and further ameliorates emphysema progression in mice following cigarette smoke exposure [54]. However, the impact of *miR-23a-3p* on EPCs in BPD was not understood. In contrast to prior analyses that identified a variable response of mature endothelial cells to *miR-23a-3p* in different disease contexts, this study demonstrates that hyperoxic macrophages release EV-encapsulated *miR-23a-3p* to induce EPC loss and impair endothelial function in the differentiated progeny. Therefore, the effects of *miR-23a-3p* appear to be context-dependent and distinct between progenitor and mature endothelial fractions.

A search for putative targets of *miR-23a-3p* also revealed many candidate genes, including *PTEN*, which has been reported to be a crucial regulator of haematopoietic stem and progenitor cell (HSPC) maintenance and that, upon inactivation or deletion, resulting in HSPC exhaustion [40, 41]. Our study for the first time demonstrated that hyperoxia-induced *miR-23a-3p* overexpression inhibits PTEN expression in mouse BPD lung endothelium, and this mechanism also applies to human CD34⁺ EPC progeny. A number of strategies, including PTEN protein delivery, miRNA targeting, and gene editing, have been employed in pre-clinical studies to improve PTEN expression [55]. However, given that the therapeutic PTEN protein tend to degrade and deliver

with low membrane permeability, as well as the short-comings of direct gene editing in introducing undesired immunogenicity and non-specific genetic modification [55], miRNA targeting could offer an expedient and economical option from a clinical and practical perspective. Moreover, our findings of antagomiR-23a-3p capable of targeting lung endothelial cells in BPD mice and improving PTEN expression further support for the therapeutic potential of antagomiR-23a-3p to treat BPD.

Faithful modeling of human BPD de novo has been difficult to achieve, therefore, the role of macrophage signals in tailoring the phenotypic and functional outputs of EPCs in human cells remains poorly understood. Here, we used an in vitro macrophage polarization system from normal human monocytes isolated directly from CB and further exposed the differentiated macrophages to hyperoxia, mimicking hyperoxia-exposed macrophages in BPD. In addition, our in vitro culture system initiated with CB-derived CD34$^+$ EPCs, demonstrates a phenotypically and functionally defined hierarchical system of cells with decreasing self-sustaining potential during ex vivo culture, which is similar to that characteristic of neonatal vascularization wherein EPCs are able to replenish themselves and to differentiate into mature endothelial cells. Furthermore, our use of CB cellular source to generate macrophages and EPCs more closely resemble neonatal lung macrophages and EPCs compared to those derived from adult peripheral blood. These features of our in vitro models thus make it possible to directly interrogate and manipulate the mediators of intercellular communications between human neonatal macrophages and EPCs, and extend prior observations made in mice, where many key pathways are not well conserved as compared to humans.

We acknowledge that our study has limitations. First, our findings are mainly based on the use of in vitro culture system developed from human CB monocyte-polarized macrophages and CD34$^+$ EPCs, which do not adequately model the human lung environment where complex interplay between inflammatory infiltration and surrounding tissue niche are involved. Second, although our study focused on microRNAs, it is possible that other cargo molecules, such as proteins, lipids, and other RNA species in hyperoxic macrophage-derived EVs may affect intercellular communication differently than microRNAs. Future studies will be required to delineate the contribution of each component of hyperoxic macrophage-derived EVs in governing EPC maintenance. Moreover, because large-scale production of EVs, appropriate cell types to use for EV production, optimal cell culture conditions, loading techniques, and determination of loaded EV toxicology remain challenging, therefore, we only administered antagomiR-23a-3p in vivo to assess whether BPD outcome could be improved by silencing *miR-23a-3p* expression in BPD mice. Last, the exact mechanism underlying the suppressive effects of EV-transmitted *miR-23a-3p* was not explored in depth in our study. Future studies could further investigate the mechanism of EV-transmitted miR-23a-3p/PTEN axis to gain a better understanding of how hyperoxic macrophage-derived EVs inhibit maintenance and endothelial capacity of EPCs and identify other potential targets for therapeutic intervention.

Conclusions

In conclusion, we demonstrate that hyperoxia activates human neonatal macrophages to secrete EV-encapsulated *miR-23a-3p* to induce EPC exhaustion, and silencing *miR-23a-3p* expression in BPD mice improves pulmonary EPC maintenance, ameliorates impaired vascularization and arrested alveolarization caused by hyperoxia. This study thus links a macrophage-derived EV-transmitted miRNA to the regulation of EPCs, and open up an avenue to develop therapeutic strategies for EPC maintenance in BPD.

Supplementary Information

The online version contains supplementary material available at https://doi.org/10.1186/s13287-024-03920-z.

Supplementary Material 1.

Author contributions
X.C. conceived the project; X.W. and X.C. designed the experiments; X.W., Y.F., Y.Z., D.H., L.Y., and Z.H. performed experiments; X.W., B.L. and X.C. analyzed data and interpreted the results; X.W. wrote the manuscript; B.L. and X.C. reviewed and revised the manuscript, and C.Y. provided technical expertise and intellectual contributions.

Availability of data and materials
miRNA sequencing data have been deposited into the CNGB Sequence Archive (CNSA) [33] of China National GeneBank Database (CNGBdb) [34] with accession number CNP 0005647. All data shown in this work are available from the corresponding author upon request.

Wang *et al. Stem Cell Research & Therapy*   (2024) 15:295

Page 21 of 22

Declarations

Ethics approval and consent to participate

Human discarded normal cord blood samples (CB) and tracheal aspirates (TA) of preterm infants with gestational age at birth ≤ 27 weeks were collected after obtaining consent from the parents and the study was approved by the Ethics Committee of the Shenzhen Maternity & Child Healthcare Hospital. The title of approved study is "Investigating the molecular mechanisms by which M1 macrophages-derived extracellular vesicles modulate EPCs to impair vascular development in BPD lungs via the miR-663a-JUND axis (M1型巨噬细胞外泌体通过miR-663a-JUND轴调控EPC在BPD肺血管生成障碍中的机制研究)", and date of approval is May 17th, 2021 (Approval number: SFYLS (2021) 020). All animal experiments were performed in accordance with approved protocols by the Institutional Animal Care and Use Committee (IACUC) of Shenzhen Institutes of Advanced Technology (SIAT) of the Chinese Academy of Science (CAS) and were reported in line with the ARRIVE guidelines 2.0. (1) Title of the approved project: Investigating the molecular mechanisms by which M1 macrophages-derived extracellular vesicles modulate EPCs to impair vascular development in BPD lungs via the miR-663a-JUND axis (M1型巨噬细胞外泌体通过miR-663a-JUND轴调控EPC在BPD肺血管生成障碍中的机制研究); (2) Name of the institutional approval committee: IACUC of SIAT of the CAS; (3) Approval number: SIAT-IACUC-190610-CXY-A0756; (4) Date of approval: June 14th, 2019.

Consent for publication

All authors confirm their consent for publication.

ARRIVE guidelines

All the experiments in this work have been reported in line with the ARRIVE guidelines 2.0.

Competing interests

The authors declare that they have no competing interests.

Author details

[1]Laboratory of Neonatology, Department of Neonatology, Shenzhen Maternity and Child Healthcare Hospital, Shenzhen 518000, China. [2]The First Clinical Medical School, Southern Medical University, Guangzhou, China. [3]Shenzhen Key Laboratory of Maternal and Child Health and Diseases, Shenzhen, China.

References

1. Thébaud B, Goss KN, Laughon M, Whitsett JA, Abman SH, Steinhorn RH, et al. Bronchopulmonary dysplasia. Nat Rev Dis Prim. 2019;5:78.
2. Baraldi E, Filippone M. Chronic lung disease after premature birth. N Engl J Med. 2007;357:1946–55. https://doi.org/10.1056/NEJMra067279.
3. Caskey S, Gough A, Rowan S, Gillespie S, Clarke J, Riley M, et al. Structural and functional lung impairment in adult survivors of bronchopulmonary dysplasia. Ann Am Thorac Soc. 2016;13:1262–70.
4. McGrath-Morrow SA, Collaco JM. Bronchopulmonary dysplasia: what are its links to COPD? Ther Adv Respir Dis. 2019;13:1753466619892492.
5. Ren X, Ustiyan V, Guo M, Wang G, Bolte C, Zhang Y, et al. Postnatal alveologenesis depends on FOXF1 signaling in c-KIT⁺ endothelial progenitor cells. Am J Respir Crit Care Med. 2019;200:1164–76.
6. Thébaud B, Abman SH. Bronchopulmonary dysplasia: Where have all the vessels gone? Roles of angiogenic growth factors in chronic lung disease. Am J Respir Crit Care Med. 2007;175:978–85.
7. Baker CD, Abman SH. Impaired pulmonary vascular development in bronchopulmonary dysplasia. Neonatology. 2015;107:344–51.
8. Liu Q, Huang X, Zhang H, Tian X, He L, Yang R, et al. C-kit + cells adopt vascular endothelial but not epithelial cell fates during lung maintenance and repair. Nat Med. 2015;21:866–8. https://doi.org/10.1038/nm.3888.
9. Fang S, Wei J, Pentinmikko N, Leinonen H, Salven P. Generation of functional blood vessels from a single c-kit+ adult vascular endothelial stem cell. PLoS Biol. 2012. https://doi.org/10.1371/journal.pbio.1001407.
10. Suzuki T, Suzuki S, Fujino N, Ota C, Yamada M, Suzuki T, et al. c-Kit immunoexpression delineates a putative endothelial progenitor cell population in developing human lungs. Am J Physiol Lung Cell Mol Physiol. 2014;306:855–65.
11. Borghesi A, Massa M, Campanelli R, Bollani L, Tzialla C, Figar TA, et al. Circulating endothelial progenitor cells in preterm infants with bronchopulmonary dysplasia. Am J Respir Crit Care Med. 2009;180:540–6.
12. Baker CD, Balasubramaniam V, Mourani PM, Sontag MK, Black CP, Ryan SL, et al. Cord blood angiogenic progenitor cells are decreased in bronchopulmonary dysplasia. Eur Respir J. 2012;40:1516–22.
13. Murohara T, Ikeda H, Duan J, Shintani S, Sasaki K, Eguchi H, et al. Transplanted cord blood-derived endothelial precursor cells augment postnatal neovascularization. J Clin Invest. 2000;105:1527–36.
14. Leal V, Ribeiro CF, Oliveiros B, António N, Silva S. Intrinsic vascular repair by endothelial progenitor cells in acute coronary syndromes: an update overview. Stem Cell Rev Rep. 2019;15:35–47.
15. Hassanpour M, Salybekov AA, Kobayashi S, Asahara T. CD34 positive cells as endothelial progenitor cells in biology and medicine. Front Cell Dev Biol. 2023;11:1–16.
16. Clement A, Chadelat K, Sardet A, Grimfeld A, Tournier G. Alveolar macrophage status in bronchopulmonary dysplasia. Pediatr Res. 1988;23:470–3.
17. Kalymbetova TV, Selvakumar B, Rodríguez-Castillo JA, Gunjak M, Malainou C, Heindl MR, et al. Resident alveolar macrophages are master regulators of arrested alveolarization in experimental bronchopulmonary dysplasia. J Pathol. 2018;245:153–9.
18. Hirani D, Alvira CM, Danopoulos S, Milla C, Donato M, Tian L, et al. Macrophage-derived IL-6 trans-signaling as a novel target in the pathogenesis of bronchopulmonary dysplasia. Eur Respir J. 2021. Available from: http://www.ncbi.nlm.nih.gov/pubmed/34446466
19. Sahoo D, Zaramela LS, Hernandez GE, Mai U, Taheri S, Dang D, et al. Transcriptional profiling of lung macrophages identifies a predictive signature for inflammatory lung disease in preterm infants. Commun Biol. 2020;3:1–12.
20. Martin P, Gurevich DB. Macrophage regulation of angiogenesis in health and disease. Semin Cell Dev Biol. 2021;119:101–10. https://doi.org/10.1016/j.semcdb.2021.06.010.
21. Ye J, Liu X. Macrophage-derived small extracellular vesicles in multiple diseases: biogenesis, function, and therapeutic applications. Front Cell Dev Biol. 2022;10:1–22.
22. Saha S, Aranda E, Hayakawa Y, Bhanja P, Atay S, Brodin NP, et al. Macrophage-derived extracellular vesicle-packaged WNTs rescue intestinal stem cells and enhance survival after radiation injury. Nat Commun. 2016;7:1–16. https://doi.org/10.1038/ncomms13096.
23. Van Niel G, D'Angelo G, Raposo G. Shedding light on the cell biology of extracellular vesicles. Nat Rev Mol Cell Biol. 2018;19:213–28. https://doi.org/10.1038/nrm.2017.125.
24. Mahida RY, Price J, Lugg ST, Li H, Parekh D, Scott A, et al. CD14-positive extracellular vesicles in bronchoalveolar lavage fluid as a new biomarker of acute respiratory distress syndrome. Am J Physiol Lung Cell Mol Physiol. 2022;322:L617–24.
25. Gou Z, Yang H, Wang R, Wang S, Chen Q, Liu Z, et al. A new frontier in precision medicine: Exploring the role of extracellular vesicles in chronic obstructive pulmonary disease. Biomed Pharmacother. 2024;174:116443. https://doi.org/10.1016/j.biopha.2024.116443.
26. Lal CV, Olave N, Travers C, Rezonzew G, Dolma K, Simpson A, et al. Exosomal microRNA predicts and protects against severe bronchopulmonary dysplasia in extremely premature infants. JCI Insight. 2018;3:e93994.
27. Kornilov R, Puhka M, Mannerström B, Hiidenmaa H, Peltoniemi H, Siljander P, et al. Efficient ultrafiltration-based protocol to deplete extracellular vesicles from fetal bovine serum. J Extracell Vesicles. 2018;7:1422674. https://doi.org/10.1080/20013078.2017.1422674.
28. Ravishankar P, Zeballos MA, Balachandran K. Isolation of endothelial progenitor cells from human umbilical cord blood. J Vis Exp. 2017;2017:1–9.
29. Wang X, Liu Y, Han D, Zhong J, Yang C, Chen X. Dose-dependent immunomodulatory effects of metformin on human neonatal monocyte-derived macrophages. Cell Immunol. 2022;377:104557. https://doi.org/10.1016/j.cellimm.2022.104557.
30. Arnaoutova I, Kleinman HK. In vitro angiogenesis: Endothelial cell tube formation on gelled basement membrane extract. Nat Protoc. 2010;5:628–35. https://doi.org/10.1038/nprot.2010.6.

31. Chen Y, Chen Y, Shi C, Huang Z, Zhang Y, Li S, et al. SOAPnuke: a MapReduce acceleration-supported software for integrated quality control and preprocessing of high-throughput sequencing data. Gigascience. 2018;7:1–6.

32. Langmead B, Trapnell C, Pop M, Salzberg SL. Ultrafast and memory-efficient alignment of short DNA sequences to the human genome. Genome Biol. 2009;10:1–10.

33. Guo X, Chen F, Gao F, Li L, Liu K, You L, et al. CNSA: A data repository for archiving omics data. Database. 2020;2020:1–6.

34. Chen FZ, You LJ, Yang F, Wang LN, Guo XQ, Gao F, et al. CNGBdb: China National GeneBank DataBase. Yi Chuan Hered. 2020;42:799–809.

35. Anyanwu AC, Kelley Bentley J, Popova AP, Malas O, Alghanem H, Goldsmith AM, et al. Suppression of inflammatory cell trafficking and alveolar simplification by the heme oxygenase-1 product carbon monoxide. Am J Physiol Lung Cell Mol Physiol. 2014;306:L749–63.

36. Masuda H, Alev C, Akimaru H, Ito R, Shizuno T, Kobori M, et al. Methodological development of a clonogenic assay to determine endothelial progenitor cell potential. Circ Res. 2011;109:20–37.

37. Xi Y, Wang Y. Insight Into the roles of non-coding RNA in bronchopulmonary dysplasia. Front Med. 2021;8:1–8.

38. Hu H, Dong L, Bu Z, Shen Y, Luo J, Zhang H, et al. miR-23a-3p-abundant small extracellular vesicles released from Gelma/nanoclay hydrogel for cartilage regeneration. J Extracell Vesicles. 2020;9:1778883. https://doi.org/10.1080/20013078.2020.1778883.

39. Hu H, Zhang H, Bu Z, Liu Z, Lv F, Pan M, et al. Small extracellular vesicles released from bioglass/hydrogel scaffold promote vascularized bone regeneration by transferring miR-23a-3p. Int J Nanomedicine. 2022;17:6201–20.

40. Yilmaz ÖH, Valdez R, Theisen BK, Guo W, Ferguson DO, Wu H, et al. Pten dependence distinguishes haematopoietic stem cells from leukaemia-initiating cells. Nature. 2006;441:475–82.

41. Zhang J, Grindley JC, Yin T, Jayasinghe S, He XC, Ross JT, et al. PTEN maintains haematopoietic stem cells and acts in lineage choice and leukaemia prevention. Nature. 2006;441:518–22.

42. Wang G, Wen B, Deng Z, Zhang Y, Kolesnichenko OA, Ustiyan V, et al. Endothelial progenitor cells stimulate neonatal lung angiogenesis through FOXF1-mediated activation of BMP9/ACVRL1 signaling. Nat Commun. 2022;13:2080.

43. Yi JS, Cox MA, Zajac AJ. T-cell exhaustion: characteristics, causes and conversion. Immunology. 2010;129:474–81.

44. Syed MA, Bhandari V. Hyperoxia exacerbates postnatal inflammation-induced lung injury in neonatal BRP-39 null mutant mice promoting the M1 macrophage phenotype. Mediators Inflamm. 2013;2013:457189.

45. Liao J, Kapadia VS, Brown LS, Cheong N, Longoria C, Mija D, et al. The NLRP3 inflammasome is critically involved in the development of bronchopulmonary dysplasia. Nat Commun. 2015;6:8977.

46. Hirani DV, Thielen F, Mansouri S, Danopoulos S, Vohlen C, Haznedar-Karakaya P, et al. CXCL10 deficiency limits macrophage infiltration, preserves lung matrix, and enables lung growth in bronchopulmonary dysplasia. Inflamm Regen. 2023;43:52. https://doi.org/10.1186/s41232-023-00301-6.

47. Wang J, Han Y, Huang F, Tang L, Mu J, Liang Y. Diabetic macrophage small extracellular vesicles-associated miR-503/IGF1R axis regulates endothelial cell function and affects wound healing. Front Immunol. 2023;14:1–18.

48. Wang N, Tan HY, Feng YG, Zhang C, Chen F, Feng Y. microRNA-23a in human cancer: Its roles, mechanisms and therapeutic relevance. Cancers (Basel). 2019;11:1–22.

49. Wang S, Sun Y, Yao L, Xing Y, Yang H, Ma Q. The role of microRNA-23a-3p in the progression of human aging process by targeting FOXO3a. Mol Biotechnol. 2024;66:277–87. https://doi.org/10.1007/s12033-023-00746-7.

50. Sheng S, Zou M, Yang Y, Guan M, Ren S, Wang X, et al. miR-23a-3p regulates the inflammatory response and fibrosis in diabetic kidney disease by targeting early growth response 1. Vitro Cell Dev Biol Anim. 2021;57:763–74.

51. Zhou C, Bei J, Qiu Y, Chang Q, Nyong E, Vasilakis N, et al. Exosomally targeting microRNA23a ameliorates microvascular endothelial barrier dysfunction following rickettsial infection. Front Immunol. 2022;13:1–11.

52. Lee Y, Kim SJ, Choo J, Heo G, Yoo JW, Jung Y, et al. MiR-23a-3p is a key regulator of IL-17C-induced tumor angiogenesis in colorectal cancer. Cells. 2020;9:1363.

53. Oikawa S, Wada S, Lee M, Maeda S, Akimoto T. Role of endothelial microRNA-23 clusters in angiogenesis in vivo. Am J Physiol Hear Circ Physiol. 2018;315:H838–46. https://doi.org/10.1152/ajpheart.00742.2017.

54. Li K, Ye X, Xu M, Xu C, Lu P, Li J, et al. MiR-23a-3p alleviates cigarette smoke extract-induced pulmonary vascular endothelial cell apoptosis by targeting DNAJB1 in emphysema. Clin Respir J. 2023;17:1223–32.

55. McLoughlin NM, Mueller C, Grossmann TN. The therapeutic potential of PTEN modulation: targeting strategies from gene to protein. Cell Chem Biol. 2018;25:19–29. https://doi.org/10.1016/j.chembiol.2017.10.009.

Publisher's Note